Supporting Information for:

Irob et al., CO_2 Fertilization to Climate Limitation: Shifting Drivers in a Dryland Forest

A. Model Parameterization and Calibration

This appendix describes the parameterization, calibration procedures, and performance evaluation of the ED2 model for *Pinus halepensis* at Yatir Forest, including vegetation parameters and data sources.

A1. Parameter adjustments

Model calibration of the most sensitive parameters for Yatir forest involved fundamental adjustments to reflect the drought-survival physiology of *P. halepensis* under arid conditions (aridity index 0.18). Calibration included iterative adjustment of physiological traits (e.g., stomatal sensitivity, phenological thresholds, respiration rates) to match observed carbon fluxes, evapotranspiration and growth trajectories. Model–data agreement was assessed at each iteration using statistical error metrics (e.g., root mean square error (RMSE), R^2) to identify the best-fitting parameter set (see section below: Data Sources and Evaluation of Model Performance). Soil moisture parameters were first calibrated independently against site observations to ensure realistic water availability. Once water balance was constrained, all flux- and growth-related vegetation parameters were calibrated jointly. Afterwards, we independently validated tree growth by comparing simulated annual DBH growth rates with observed growth measurements (Fig. S3).

Key parameter adjustments included: (1) drastically reduced photosynthetic capacity (Vm0) and quantum efficiency to reflect chronic drought stress limitations (Grünzweig et al., 2003; Klein et al., 2011; Maseyk et al., 2008); (2) enhanced drought tolerance mechanisms including increased stomatal sensitivity to vapor pressure deficit (VPD) and elevated cavitation resistance (Choat et al., 2018; Klein et al., 2014; Preisler et al., 2019); (3) conservative carbon allocation strategies with reduced turnover rates for leaves, roots, and storage pools to maximize resource retention during extended drought periods (Klein, 2021; Piper & Fajardo, 2016); (4) restrictive growth parameters including reduced maximum leaf biomass and specific leaf area reflecting the sclerophyllous needle morphology (Klein et al., 2011; Osem & O'Hara, 2016); and (5) modified soil parameterization including increased layer resolution and adjusted texture properties to enhance water retention capacity in the water-limited environment (Preisler et al., 2019; Raz-Yaseef et al., 2012; Rotenberg & Yakir, 2010) (Table S1). Collectively, these parameter adjustments transformed the ED2 model from a growth-maximizing temperate forest system to a survival-optimized arid afforested system (Table S2).

A2. Evaluation of Model Fit

Model calibration utilized a 20-year dataset (2000–2020) from a fluxtower at Yatir Forest, combining eddy covariance measurements of both carbon (gross primary productivity (GPP), net ecosystem productivity, respiration (RECO) and water fluxes (evapotranspiration (ET) via latent heat flux (LE)) (Pastorello et al., 2020), alongside soil moisture records, observations of the forest leaf area index (LAI; 2005-2008, Sprintsin et al., 2011), and tree growth data from dendrometer and tree-ring measurements (unpublished data). Including both carbon and water fluxes allowed evaluation of model carbon-water coupling.

Model fit was evaluated using a multi-component scoring system that assessed: (1) RMSE surface layer comparisons between simulated soil moisture dynamics and measurements; (2) agreement between simulated and observed evapotranspiration (ET), evaluated through annual totals and seasonal dynamics; (3) correlation and RMSE between simulated vegetation structure and LAI observations; and (4) correlation, mean bias (average systematic deviation between simulated and observed values), and RMSE metrics for simulated vs. observed carbon fluxes (GPP, NEP, RECO, and NPP) using NT_VUT-filtered reference data. Parameter optimization followed an iterative approach testing multiple parameter combinations, with the final evaluation focusing on the three best-performing model versions. The full script to reproduce the calibration evaluation can be found in the figshare repository.

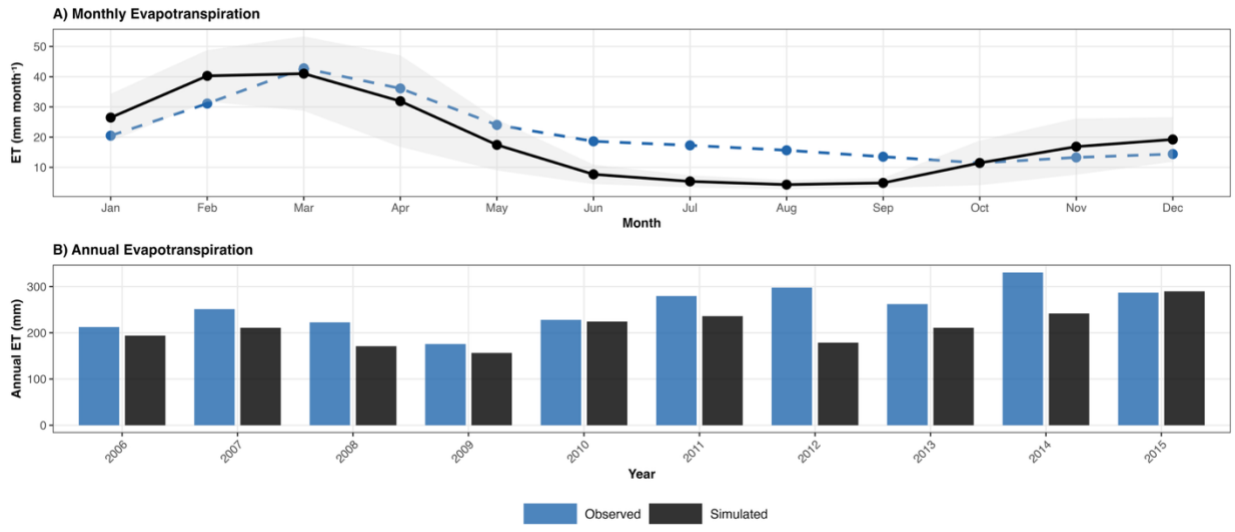

Figure S1. Comparison of mean monthly (A, 2000-2020) and annual evapotranspiration (B, 2005-2015) between observed eddy covariance measurements and simulated model outputs.

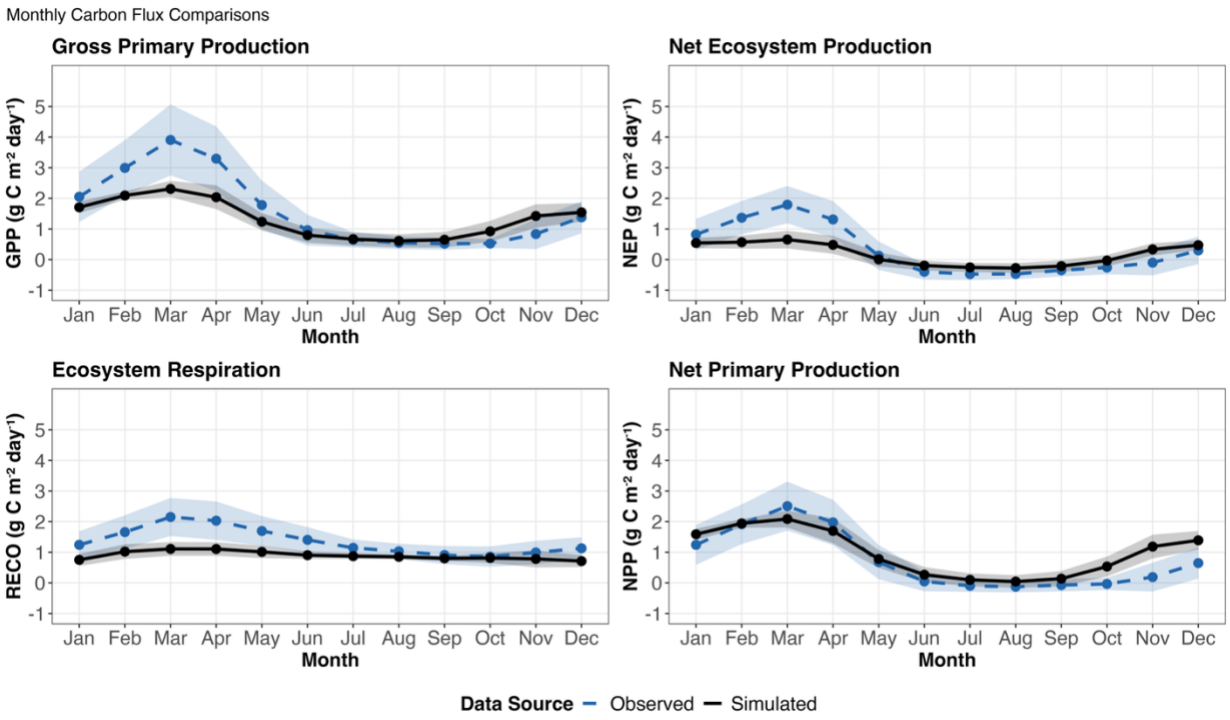

Figure S2. Monthly comparisons of carbon flux components between observed eddy covariance data (blue dashed lines) and simulated model outputs (black solid lines), averaged over 21 years (2000-2021) to characterize the typical seasonal pattern critical to Mediterranean dryland forest function. Plots shown are gross primary production (GPP), net ecosystem production (NEP), ecosystem respiration (RECO), and net primary production (NPP).

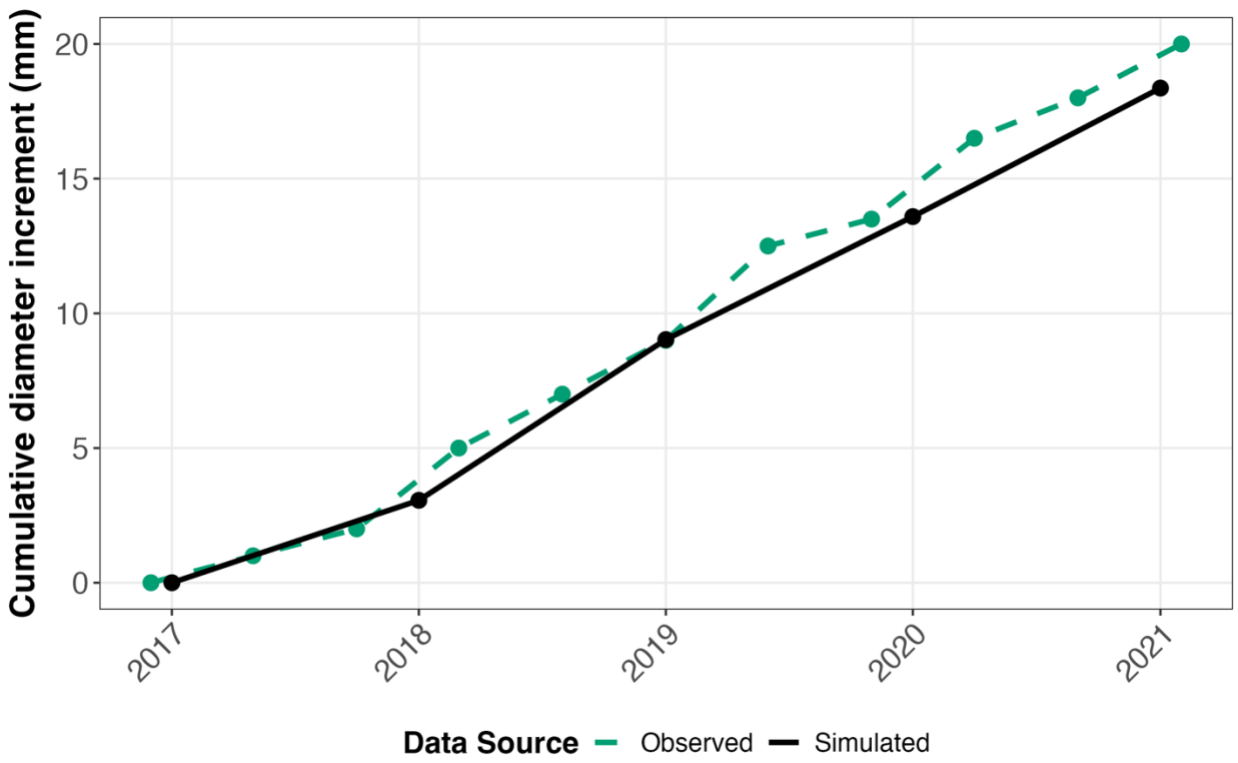

Figure S3. Validation of cumulative diameter increment (mm) from 2017 to 2021, comparing simulated stand-weighted mean DBH growth (black, solid) with dendrometer measurements from unthinned control plots at density 30 (green, dashed; Klein et al., unpublished data). The dendrometer data represent an independent validation dataset not used during model calibration.

A3. Vegetation parameters

Table S1. Complete ED2 Model Parameter Calibration for Pinus halepensis at Yatir Forest.

Parameter Category	Parameter Name	Description	Final Value	Units	Data Source / Justification	Literature Reference
Photosynthetic Capacity						
	Vm0	Maximum rate of carboxylation at 15°C[a]	21.8	μmol/m²/s	Yatir field data: 5.5–25.9 range, drought-stressed conditions	Maseyk et al. 2008, Preisler et al. 2021
	quantum_efficiency	Quantum yield of photosynthesis	0.042	–	Lower light use efficiency under Mediterranean drought stress	Calibrated within 0.04–0.08 range
	Jm0	Maximum electron transport rate at 15°C[a]	30.5	μmol/m²/s	Yatir field data: 95 μmol/m²/s, scaled for temperature	Maseyk et al. 2008

	dark_respiration_factor	Dimensionless ratio of leaf dark respiration to carboxylation capacity (Rd:Vm)[b]	0.0145	–	Minimized maintenance respiration for carbon conservation	Calibrated for drought survival
	Rd0	Dark respiration rate at 25°C[a]	0.022	μmol/m²/s	Very low dark respiration for carbon conservation	Drought adaptation literature
Water Relations						
	D0	VPD threshold for stomatal response	0.15	kPa	High VPD tolerance for Mediterranean climate	Field observations of stomatal behavior
	stomatal_slope	Sensitivity of stomata to VPD	10.5	–	Reduced stomatal responsiveness, conservative water use	Field data: –0.051, scaled appropriately
	cuticular_cond	Minimum conductance through cuticle	23.0	μmol/m²/s	Extremely low cuticular conductance from thick needle cuticles	Maseyk et al. 2008: 18.61
	water_conductance	Water transport per unit root biomass	0.0042	m²/yr/kgC	Enhanced water transport efficiency per unit biomass	Calibrated for deep root systems
Leaf Morphology						
	SLA	Specific Leaf Area	6.3	m²/kg	Low SLA reflecting thick, sclerophyllous needle structure	Field data: 3.5–7 m²/kg range
	leaf_turnover_rate	Rate of leaf replacement	0.42	/yr	Slow leaf turnover to maximize ROI under drought	Conifer literature values
	leaf_width	Leaf width	0.05	m	Maintained needle width from reference	Field data measurement
Allometric Relationships						
	b1Ht	Height allometry intercept	15.2	–	DBH–height relationship from field measurements	Field data calibration (Grünzweig et al. 2007)
	b2Ht	Height allometry slope	–0.048	–	Height scaling with diameter	Field data calibration (Grünzweig et al. 2007)
	hgt_min	Minimum plant height	1.5	m	Minimum recruitment size observed	Field observations

	hgt_max	Maximum plant height	18.0	m	Maximum height from field measurements	Preisler et al. 2021, Field observations
	b1Bl	Leaf biomass allometry intercept	0.26	–	Leaf biomass scaling with size	Calibrated from LAI measurements
	b2Bl	Leaf biomass allometry slope	1.31	–	Allometric scaling exponent	Leaf biomass measurements
	b1Bs_small	Small tree stem biomass intercept	0.0297	–	Stem biomass for small trees	Field biomass measurements
	b2Bs_small	Small tree stem biomass slope	2.64	–	Stem biomass scaling exponent	Allometric relationships
	dbh_crit	Critical DBH for size classes	35.0	cm	Size threshold for allometric transitions	Large tree observations
	min_dbh	Minimum DBH for reproduction	0.40	cm	Smallest reproductive individuals	Field reproductive surveys
Carbon Allocation						
	growth_resp_factor	Proportion of growth respiration	0.26	–	Higher growth costs under water stress	Drought stress physiology
	root_turnover_rate	Root mortality rate	0.057	/yr	Very slow root turnover for maintaining deep water access	Deep root system maintenance
	storage_turnover_rate	Rate of stored carbon use	0.055	/yr	Slow storage mobilization for drought survival strategy	Drought survival literature
	f_labile_leaf	Fraction of labile carbon in leaves	0.70	–	Moderate labile carbon for stress response flexibility	Carbon allocation theory
Vegetation Dynamics						
	laimax_plastic	Maximum plastic LAI	1.65	m^2/m^2	Field LAI observations: 1.2–2.2 range, drought-limited	Sprintsin et al. 2007, 2011
	q	Growth efficiency parameter	1.5	–	Slightly enhanced growth efficiency	Calibrated for realistic growth
	leaf_grow_rate	Leaf development rate	0.028	/day	Controlled leaf development rate	Phenology calibration
	leaf_shed_rate	Leaf shedding rate	0.055	/day	Summer drought leaf shedding	Mediterranean drought response
Stress Tolerance						
	mort2	Carbon stress mortality threshold	30.0	–	High carbon stress tolerance before mortality	Drought survival observations

	cbr_severe_stress	Minimum carbon balance ratio before mortality	0.38	–	Survival threshold at 38% of optimal carbon balance	Extreme drought survival data
Decomposition						
	decay_rate_fsc	Fast soil carbon decay rate	0.012	/yr	Soil carbon: 4.9 kg/m² to 0.5 m depth in 2016	Qubaja et al. 2020
	decay_rate_stsc	Slow soil carbon decay	0.0053	/yr	Long-term soil carbon stability	Qubaja et al. 2020
	rh_decay_dry	Respiration decay under dry conditions	18	–	–	–
	rh_dry_smoist	Soil moisture threshold for dry conditions	0.12	m³/m³	Lower moisture threshold for Mediterranean soils	Regional soil characteristics

[a] Reference temperatures follow ED2 parameter conventions (ed_state_vars.f90): Vm0 and Jm0 are specified at 15°C, while Rd0 is specified at 25°C. ED2 internally converts all parameters to 25°C for calculations (ed_params.f90). All rates are in μmol CO_2 m^{-2} s^{-1} at their respective reference temperatures.

[b] dark_respiration_factor is a dimensionless PFT-specific ratio (Rd:Vm) that defines leaf dark respiration relative to carboxylation capacity. When Rd0 is not directly specified, ED2 calculates it as: Rd0 = dark_respiration_factor × Vm0 × temperature correction factor (ed_params.f90).

A3.2. Aboveground Biomass Calculation

Aboveground biomass (AGB) was calculated from individual tree dimensions using locally derived allometric relationships. We used destructive sampling data from Grünzweig et al. (2007) to develop power-law allometric equations relating DBH to aboveground dry biomass. Because the original equations were developed for smaller trees and showed poor fit for larger individuals, we fitted separate relationships for small (DBH ≤15 cm) and large trees (DBH >15 cm):

$$AGB = a \times DBH^{b}$$

where parameters a and b differ between size classes (Table S1).
ED2 uses these allometric parameters to convert cohort-level DBH distributions to biomass. Total stand AGB is calculated by summing across all cohorts weighted by their density. This approach ensures that simulated AGB emerges from validated demographic processes (individual tree growth, mortality) rather than being directly calibrated, following standard practice in process-based vegetation modeling (Chang et al., 2025; Antonarakis et al., 2011).

Data Sources

Primary Field Data:

- Maseyk et al. 2008: Photosynthetic parameters, stomatal conductance, cuticular conductance
- Preisler et al. 2021: Water potential, physiological stress responses
- Sprintsin et al., 2007, 2011: LAI measurements, canopy structure
- Qubaja et al., 2020: Soil carbon pools and dynamics

Parameter Ranges Informed By:

- Rog et al., 2021: Recent physiological measurements
- Klein et al., 2011, 2014: Water relations and drought response
- Lapidot et al., 2019: Stomatal conductance ranges
- Llusia et al., 2016: Multi-site Mediterranean pine data

Units and Scaling:

- Temperature-dependent parameters adjusted to ED2's reference temperatures
- Conductance units converted between measurement scales (mol m^{-2} s^{-1} to μmol m^{-2} s^{-1})
- Time scales standardized to annual rates where appropriate

References for Tables S2-S3:

- Johnston, 2021: California Tonzi Range
- Antonarakis et al., 2022: California Sierra Nevada
- Pandit et al., 2019: Sagebrush-steppe ecosystems in western North America
- Zhang et al., 2022: Puerto Rico Tropical Forest

B. Model Outputs: Extended Results

This appendix presents extended model outputs including forest structure dynamics, drought sensitivity analysis, CO_2 fertilization effects, and imposed model constraints.

B1. Forest Structure

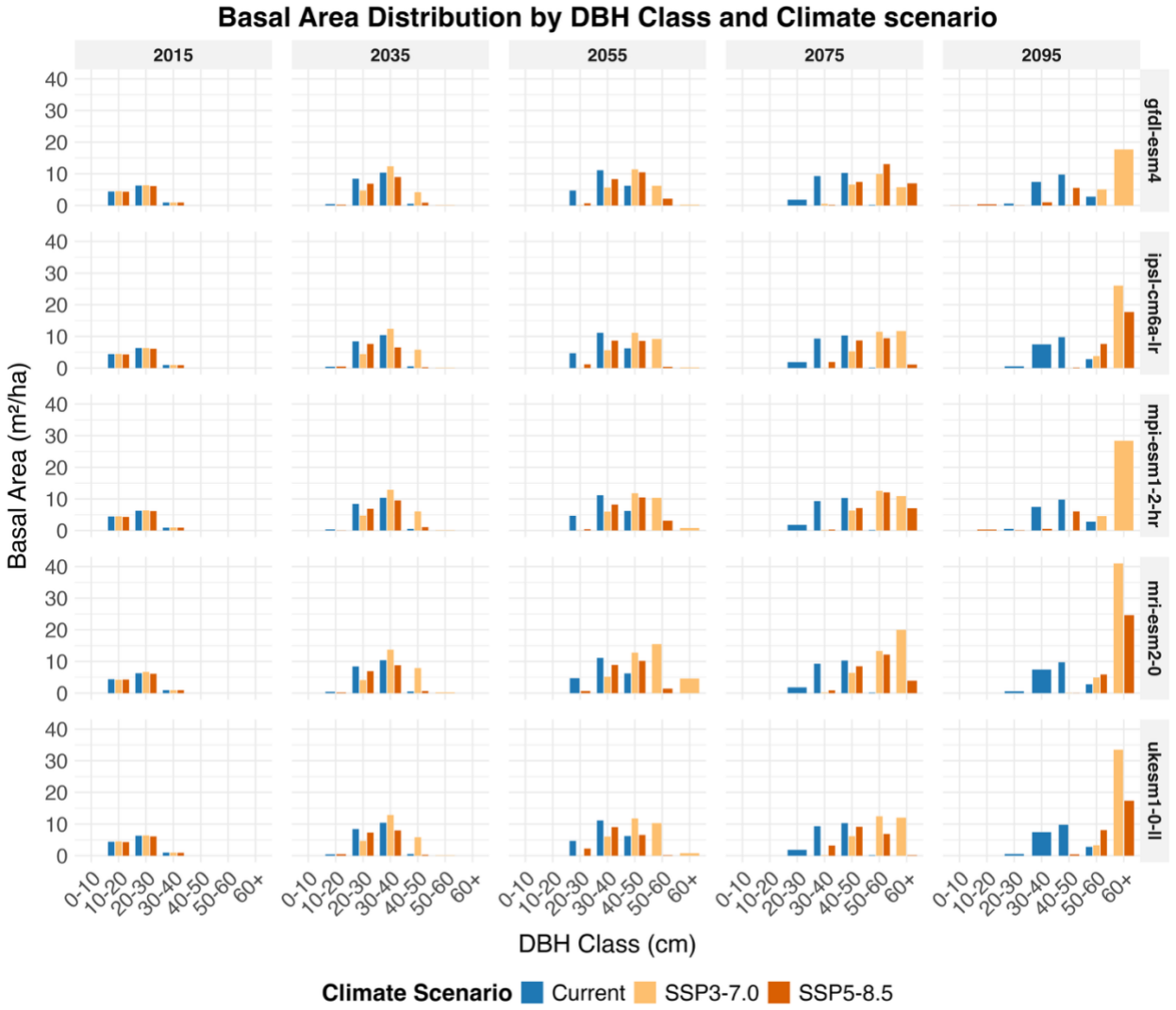

Figure S4. Basal area distribution by DBH class across climate scenarios, models, and time periods. Bars show mean basal area (m^2 ha^{-1}) per DBH class (0–10 cm to 40–50 cm) for each scenario (current: blue; SSP3-7.0: orange; SSP5-8.5: red), averaged across replicate simulations for each climate model. Columns represent simulation years (2015–2095, 20-year intervals); rows represent global climate models (GFDL-ESM4, IPSL-CM6A-LR, MPI-ESM1-2-HR, MRI-ESM2-0, UKESM1-0-LL). The current climate bar serves as a shared reference in all panels, while future scenarios reflect model-specific climate projections

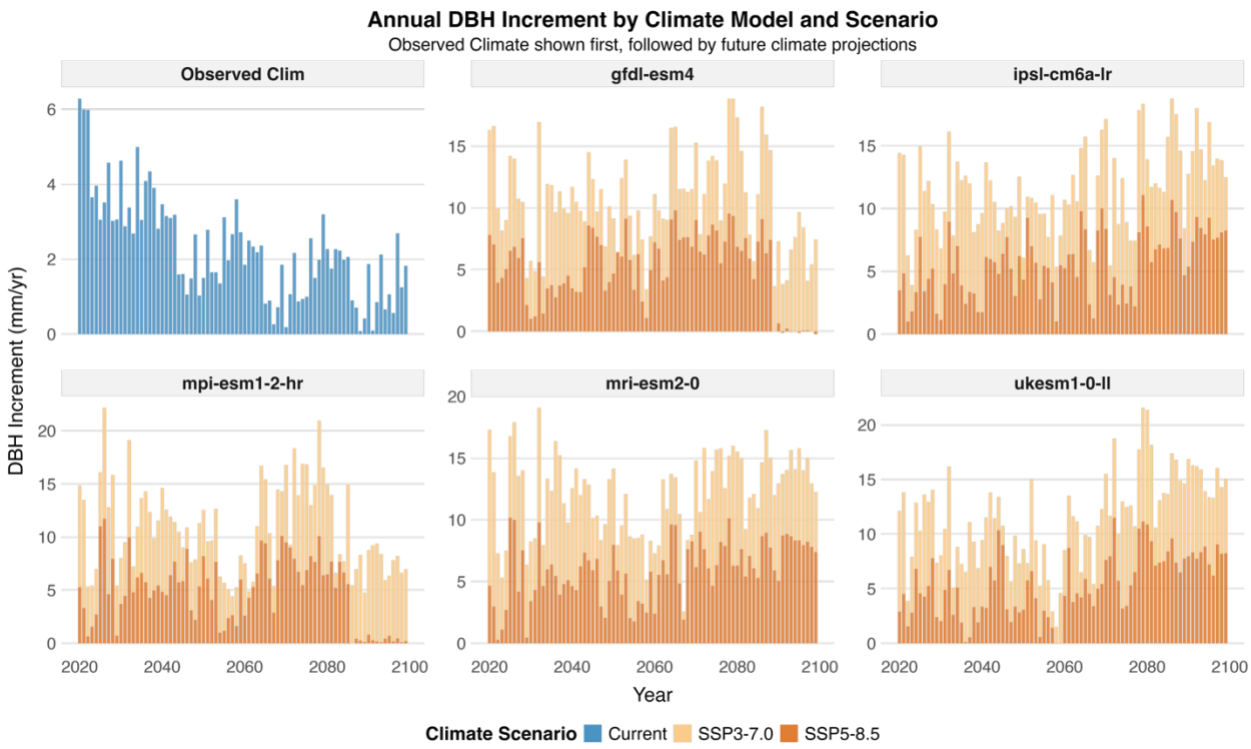

Figure S5. Annual DBH increment responses to climate scenarios across Earth system models. Observed climate (top-left) provides a baseline for comparison with moderate (SSP3-7.0) and high (SSP5-8.5) warming projections, showing generally enhanced growth under warmer conditions.

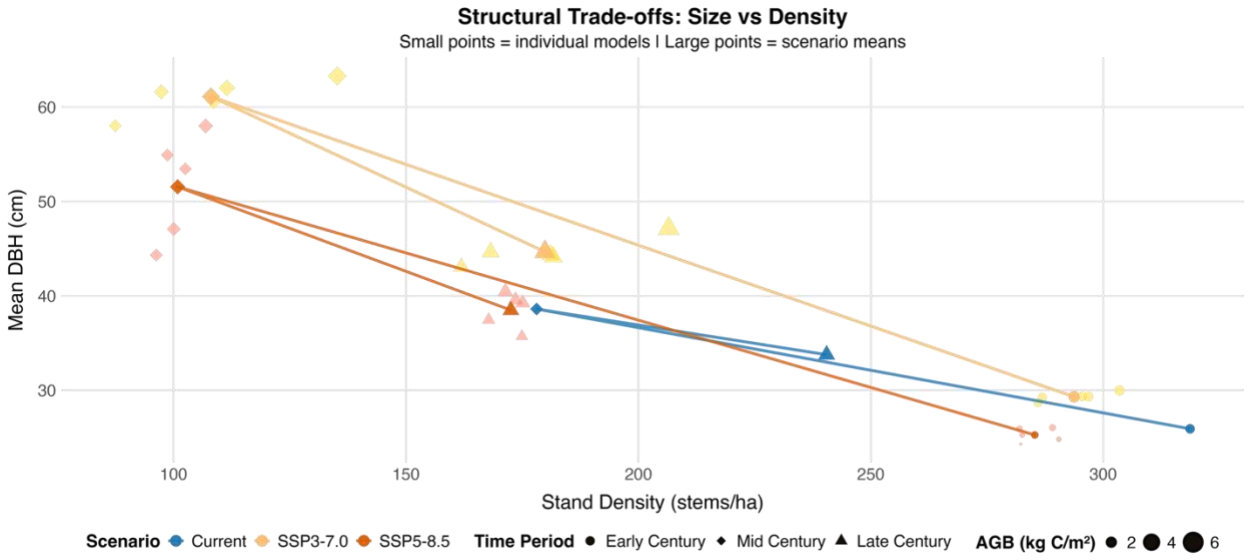

Figure S6. End-of-century relationships between mean DBH and total annual rainfall across scenarios, with marker shapes representing different years and model members.

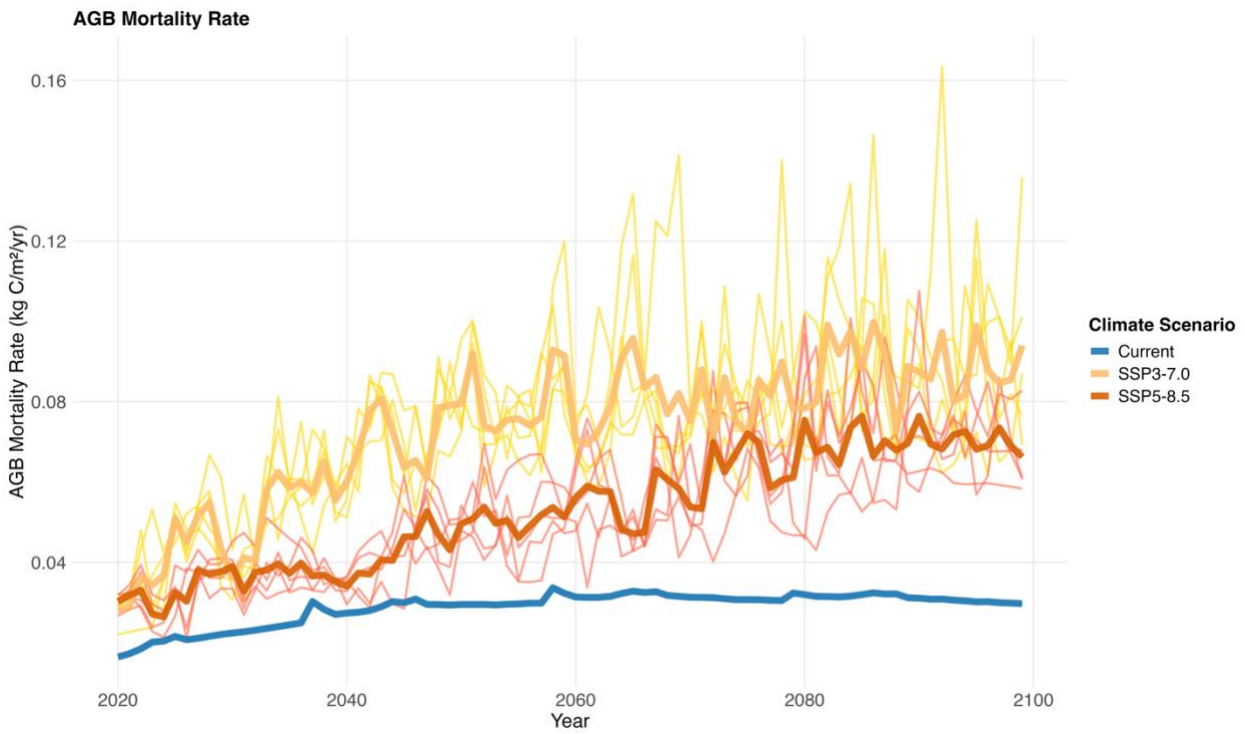

Figure S7. Time series of above ground biomass mortality rate of a Mediterranean pine forest from 2020 to 2100 under current (blue), moderate (light orange), and high-emission (dark orange) scenarios. Each thick line represents the mean of five models per scenario (thin lines). A: Temporal trajectories of forest structural responses under different climate scenarios.

Table S2a. Timing of sustained decline across response variables and climate scenarios.

Scenario	Metric	Models with decline (%)	Mean onset year ± SD
SSP3-7.0	NEP	100% (5/5)	2037 ± 0
	WUE	100% (5/5)	2042 ± 9
	LAI	100% (5/5)	2039 ± 3
	AGB Growth	100% (5/5)	2037 ± 0
SSP5-8.5	NEP	60% (3/5)	2053 ± 16
	WUE	80% (4/5)	2041 ± 10
	LAI	100% (5/5)	2049 ± 7
	AGB Growth	80% (4/5)	2048 ± 16

Note: Decline onset defined as first year of sustained negative 15-year rolling trend ($p < 0.1$), with analysis beginning from 2030 to avoid initialization artifacts. Under SSP3-7.0, all metrics declined near-simultaneously (~2037), while SSP5-8.5 showed greater temporal variability and model divergence.

Table S2b. Early warning lags.

Scenario	Models with both events	Functional decline onset	AGB stagnation onset	Warning window
SSP3-7.0	100% (5/5)	2037	2055 ± 6	12-25 yr (mean 18 ± 6)

SSP5-8.5	40% (2/5)	2044	2067 ± 21	7-37 yr (mean 22 ± 21)

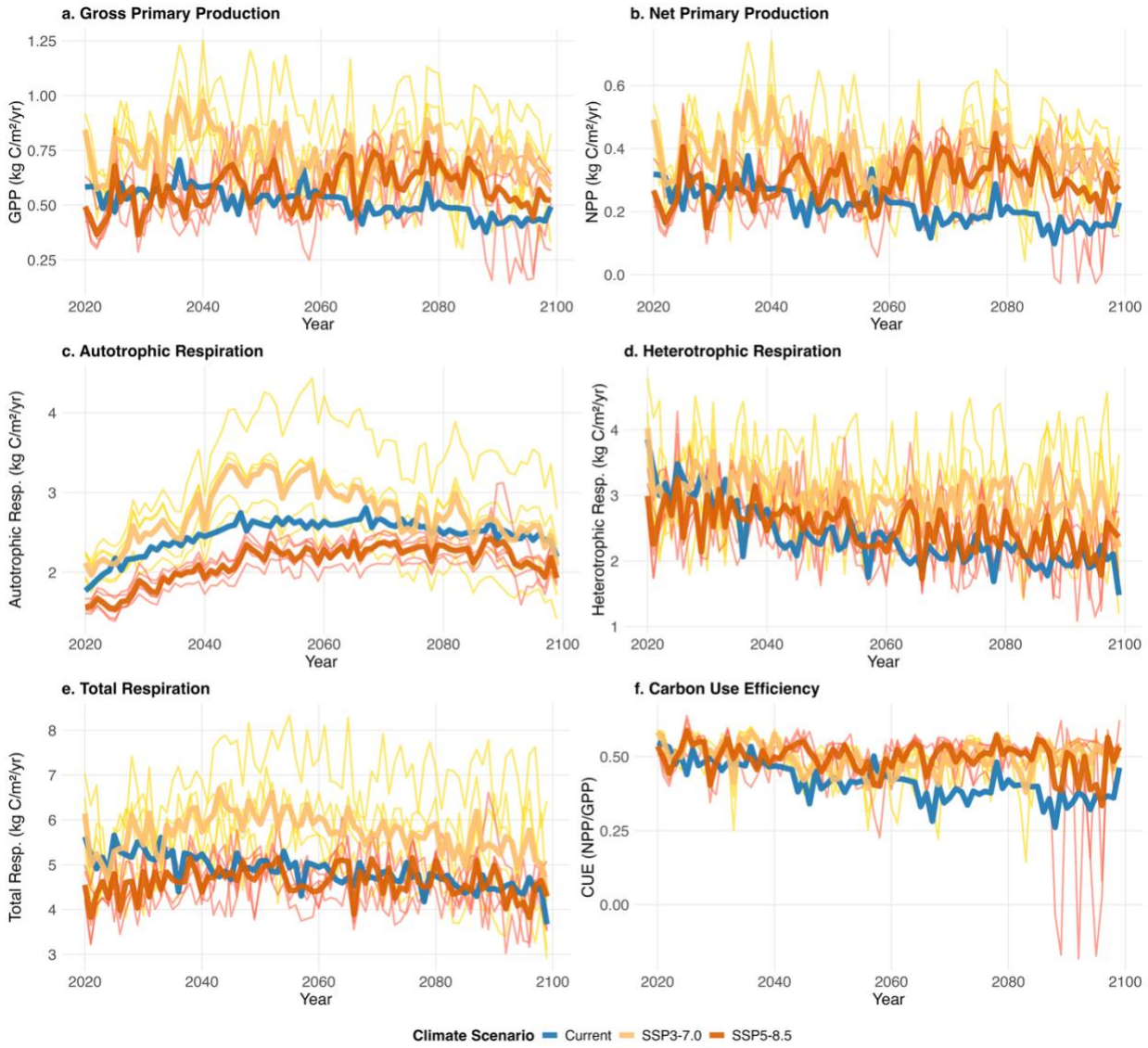

Fig. S8: Time series of key carbon fluxes of a dryland pine forest from 2020-2100 under current (blue), and two high emission scenarios, SSP3-7.0 (light orange), and SSP5-8.5 (dark orange) scenarios. Each thick lines represents the mean of five models per scenario (thin lines). (a) gross primary production (GPP), (b) net primary production (NPP), (c) autotrophic respiration (d) heterotrophic respiration, (e) total respiration and (f) carbon use efficiency (CUE).

CO_2 Fertilization–Climate Stress Interaction Analysis

To investigate how temperature and water stress either enhance or constrain the effects of CO_2 fertilization, we analyzed the interactions among the three effects. CO_2 concentrations were defined using evenly spaced bins that span the full range of projected concentrations (low: <450 ppm, medium: 450–600 ppm, high: 600–800 ppm, very high: >800 ppm), mean annual temperature conditions (cool: <19.2°C, moderate: 19.2–20.2°C, warm: 20.2–23.3°C, hot: >23.3°C), and soil water stress levels based on the soil moisture content (low stress: >17 vol%, moderate stress: 14–17 vol%, high stress: <14 vol%). Soil moisture and temperature thresholds were derived from historical summary quantiles (25th–75th percentiles) to define stress relative to current conditions, while CO_2 and temperature classes were chosen to represent distinct, interpretable forcing and thermal regimes across the projection range. We used monthly model outputs of forest structural and functional responses (DBH, AGB, AGB growth rate, LAI, NEP, and WUE) and grouped them according to the abovementioned environmental classes. For each combination of CO_2, temperature, and water class with ≥10 monthly data points, we calculated the mean ecosystem response to ensure statistical robustness.

CO_2 Drives Forest Responses with Limited Temperature Modulation

CO_2 was the dominant driver across both structural and functional variables, with limited temperature modulation within CO_2 levels (Fig. 5). Under SSP5-8.5, cool conditions were largely absent at high CO_2 levels, showing the narrowed climate space under severe warming. Structural variables (Total AGB, Mean DBH, AGB Growth) increased consistently with CO_2 enrichment under both high emission scenarios, with temperature categories showing largely overlapping responses within each CO_2 level (Fig. 5a). LAI declined sharply at higher CO_2 levels under SSP3-7.0. AGB growth rate showed weaker CO_2 sensitivity in both high emission scenarios.

Functional responses showed an initial increase from current to moderately elevated CO_2 but limited further gains at higher concentrations (Fig. 5b). NEP increased from Current to Moderate CO_2 levels under both emission scenarios but plateaued or declined at High and Very High CO_2, where associated high temperatures limited additional fertilization benefits. WUE showed a similar pattern, with the largest gains occurring at the initial step from current to elevated CO_2. Temperature effects within CO_2 levels were generally weak and inconsistent across both structural and functional variables.

Water Availability Constrains CO_2 Fertilization at High Enrichment Levels

CO_2 was the dominant driver of structural and functional responses, with water stress effects emerging primarily at the highest CO_2 levels, though responses differed between emission scenarios (Fig. 6). Structural variables (Total AGB, Mean DBH, and AGB growth rate) increased with CO_2 enrichment under both scenarios, with water stress categories overlapping within each CO_2 level. Under SSP3-7.0, stress categories were distributed across all CO_2 levels, with no consistent separation except at Very High CO_2, where high stress tended toward lower AGB and DBH. LAI declined at higher CO_2 under SSP3-7.0, with high water stress amplifying the decline. Under SSP5-8.5, low water stress conditions were largely absent at high CO_2 levels, reflecting the narrowed climate space under severe warming, and stress-level separation was not apparent. A similar pattern appeared in the VPD analysis (Fig. S9), where VPD categories collapsed toward high values under SSP5-8.5 at elevated CO_2, suggesting co-occurrence of water and atmospheric drought precluded separation. AGB growth rate showed weaker CO_2 sensitivity in both emission scenarios, with no clear differentiation by water stress level.

Functional responses showed a similar initial increase from current to elevated CO_2 that plateaued at higher concentrations (Fig. 6b). NEP increased from current to moderate CO_2 but showed limited further gains at higher concentrations, with a small negative effect of high water stress within CO_2 levels. WUE increased with CO_2 enrichment; within CO_2 levels, high water stress tended toward higher WUE values, consistent with reduced transpiration under drought.

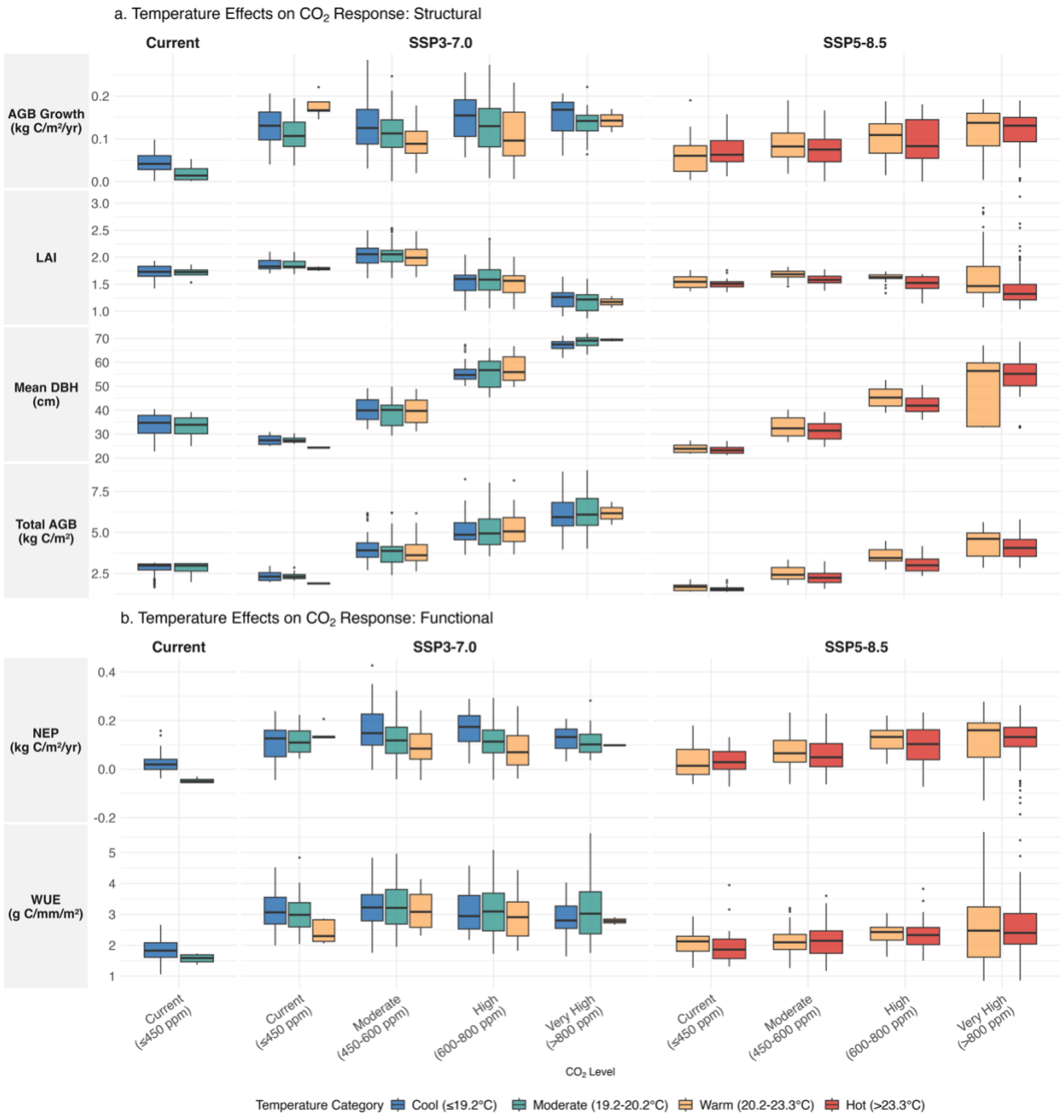

Figure S9: Interactive effects of temperature and CO_2 enrichment on (a) structural metrics (mean DBH, total AGB, AGB growth rate (LAI)) and (b) functional metrics (NEP and WUE) across three climate scenarios. Boxplots showing distributions grouped by CO_2 level and temperature category.

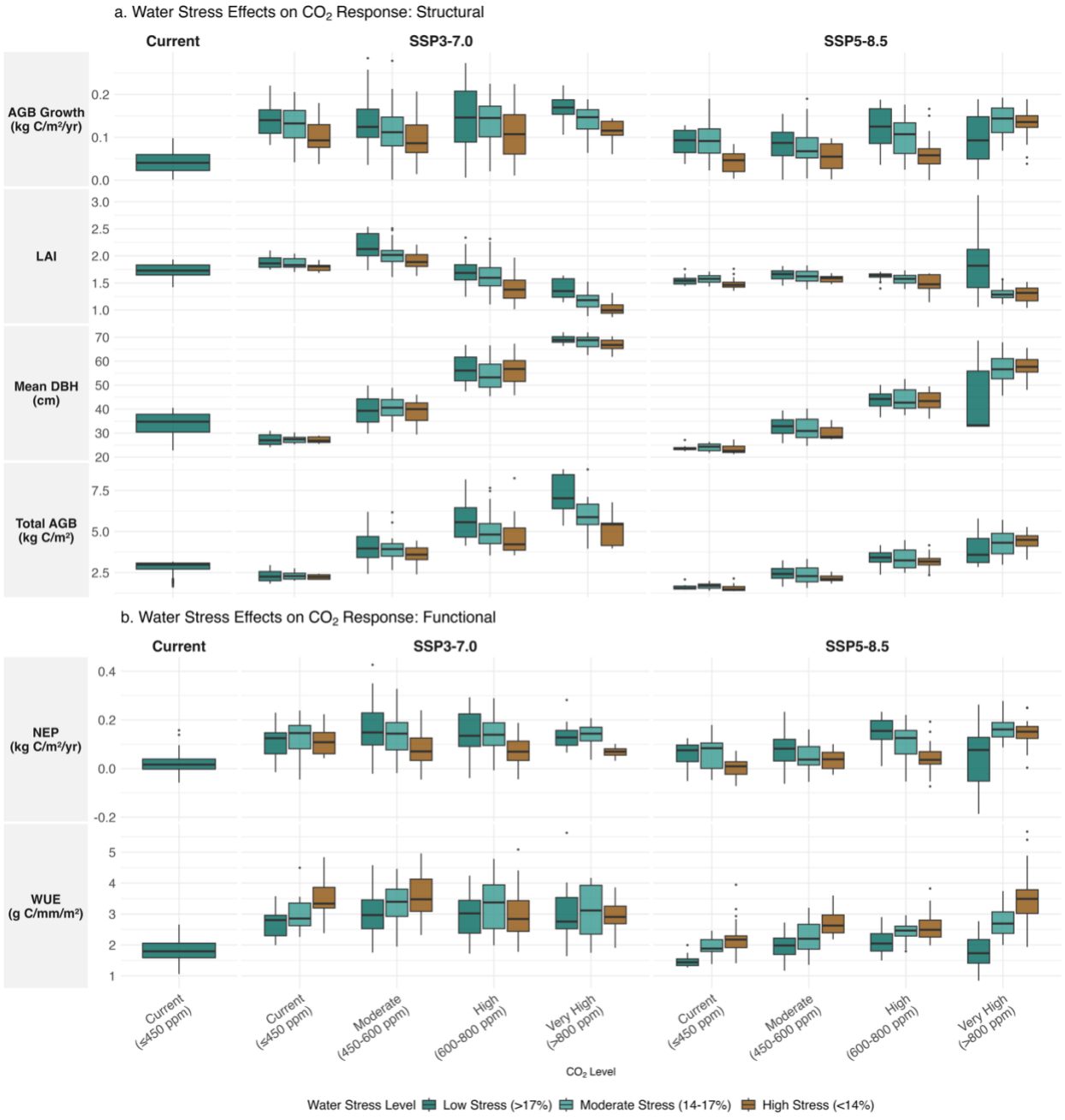

Figure S10: Interactive effects of water stress and CO_2 enrichment on (a) structural metrics (mean DBH, total AGB, AGB growth rate, LAI) and (b) functional metrics (NEP, WUE) across three climate scenarios. Boxplots showing distributions grouped by CO_2 level and water stress category (soil moisture in vol%).

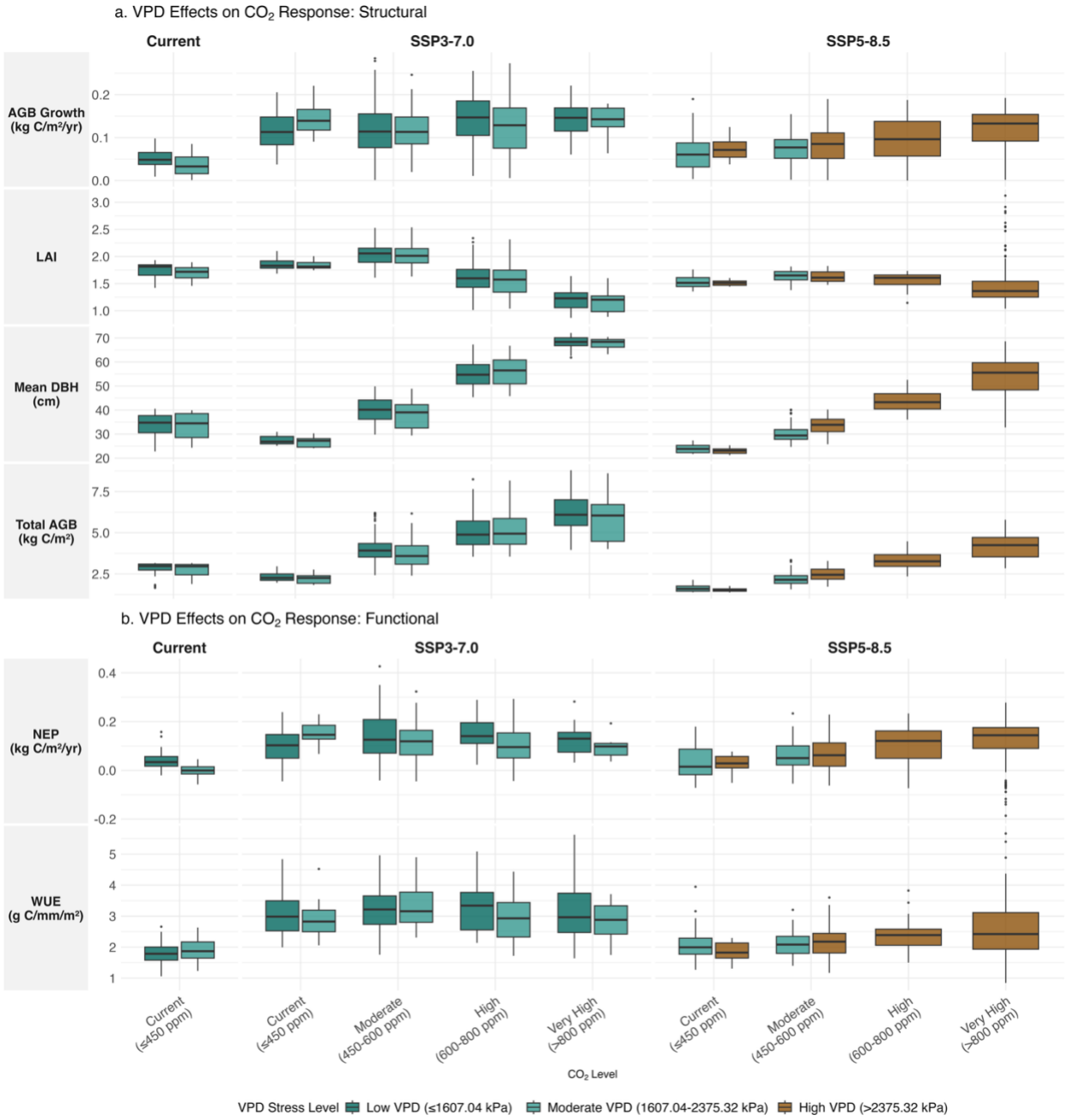

Figure S11. Effects of VPD stress on the CO_2 response. Interactive effects of water stress and CO_2 enrichment on (a) structural metrics (mean DBH, total AGB, AGB growth rate (LAI)) and (b) functional metrics (NEP, WUE) across three climate scenarios. Boxplots showing distributions grouped by CO_2 level and VPD stress category (VPD in kPa).

Atmospheric Water Demand Shows Weak CO_2 Interactions

Vapor pressure deficit (VPD), representing atmospheric water demand, showed minimal modulation of CO_2 fertilization effects across all response variables (Fig. S#). Unlike soil moisture, VPD categories did not differentiate forest responses within CO_2 levels. Structural variables (Total AGB, Mean DBH,

LAI, AGB Growth) remained nearly identical across Low, Moderate, and High VPD conditions, with CO_2 effects dominating regardless of atmospheric drying power (Fig. S8a).

Functional responses showed similarly weak VPD interactions. Net ecosystem productivity maintained consistent values across VPD categories within each CO_2 level, lacking the clear decline under high atmospheric demand that characterized soil moisture responses (Fig. S8b). Water-use efficiency increased with CO_2 enrichment but showed minimal VPD differentiation, indicating that stomatal regulation and carbon uptake responded primarily to soil water availability rather than atmospheric drying.

These patterns demonstrate that below-ground water limitation exerted stronger control over forest responses than atmospheric water demand at this semi-arid site. The weak VPD effects, contrasted with strong soil moisture interactions (Fig. 6), suggest that Yatir forest physiology and growth track root-zone water availability as the primary constraint, with atmospheric conditions playing a secondary role in modulating CO_2 fertilization benefits.

Table S3. Individual driver importance (GAM main effects, AR1-corrected). Variance explained by individual environmental drivers for each response variable across three time periods. Only significant terms ($p < 0.05$) shown, sorted by variance explained within each response-period combination. Models include first-order autoregressive (AR1) residual correlation structure grouped by simulation run.

Response	*Period*	*Driver*	*Var. Expl. (%)*	*F*	*p-value*
Mean DBH	Early	CO_2	84.5	532.06	<0.001
		Mean temperature	7.4	46.48	<0.001
		ET/Precip ratio	0.5	3.00	<0.001
		Heat stress months	0.4	2.76	0.001
		Wet season soil moisture	0.1	0.88	0.042
	Mid	CO_2	83.0	516.19	<0.001
		Heat stress months	7.2	45.07	<0.001
		Mean temperature	3.4	21.41	<0.001
		ET/Precip ratio	0.9	5.77	<0.001
		Mean soil moisture	0.4	2.74	<0.001
		Total precipitation	0.2	1.53	0.008
		Dry season soil moisture	0.2	0.98	0.009
	Late	CO_2	32.4	67.19	<0.001
		Total precipitation	6.7	13.98	<0.001
		Mean VPD	3.8	7.87	<0.001
		Mean soil moisture	3.1	6.34	<0.001
		Wet season soil moisture	2.0	4.24	<0.001

		Heat stress months	0.6	1.17	0.010
		Dry season soil moisture	0.5	1.14	0.004
Mean AGB	Early	CO_2	76.4	220.51	<0.001
		Mean temperature	3.9	11.37	<0.001
		Heat stress months	1.4	4.16	<0.001
		Total precipitation	1.1	3.14	<0.001
		Mean VPD	0.8	2.40	0.008
		ET/Precip ratio	0.5	1.57	0.014
		Wet season soil moisture	0.4	1.22	0.022
	Mid	CO_2	40.5	64.92	<0.001
		Heat stress months	15.1	24.29	<0.001
		ET/Precip ratio	5.6	9.00	<0.001
		Dry season soil moisture	4.4	7.01	<0.001
		Total precipitation	3.7	5.86	<0.001
		Mean temperature	3.6	5.84	<0.001
	Late	CO_2	26.0	31.52	<0.001
		ET/Precip ratio	9.2	11.19	<0.001
		Heat stress months	3.7	4.54	<0.001
		Dry season soil moisture	2.3	2.74	<0.001
		Mean VPD	1.5	1.84	<0.001
		Mean temperature	1.1	1.37	0.015
		Total precipitation	0.8	0.95	0.038
AGB Growth	Early	Mean temperature	32.9	26.05	<0.001
		ET/Precip ratio	27.7	21.88	<0.001
		Total precipitation	9.7	7.66	<0.001
		Wet season soil moisture	7.6	5.98	<0.001
		CO_2	4.2	3.34	<0.001
		Mean soil moisture	3.8	2.98	<0.001
	Mid	ET/Precip ratio	49.1	36.66	<0.001
		CO_2	18.4	13.76	<0.001
		Wet season soil moisture	8.1	6.09	<0.001
		Total precipitation	4.3	3.20	0.001
		Mean soil moisture	3.8	2.87	<0.001

		Mean VPD	3.0	2.27	0.001
		Heat stress months	2.6	1.95	0.005
	Late	ET/Precip ratio	40.2	37.58	<0.001
		Total precipitation	10.4	9.74	<0.001
		CO_2	4.2	3.92	<0.001
		Mean soil moisture	3.1	2.91	<0.001
		Mean temperature	2.5	2.38	<0.001
		Wet season soil moisture	0.9	0.82	0.034
Mean LAI	Early	Mean temperature	45.7	94.71	<0.001
		CO_2	37.9	78.52	<0.001
		ET/Precip ratio	2.8	5.86	<0.001
		Total precipitation	2.3	4.85	<0.001
		Wet season soil moisture	0.7	1.42	0.007
		Heat stress months	0.5	1.13	0.030
		Mean soil moisture	0.5	0.98	<0.001
		Dry season soil moisture	0.2	0.49	0.039
	Mid	CO_2	38.0	54.76	<0.001
		ET/Precip ratio	9.9	14.25	<0.001
		Heat stress months	6.6	9.54	<0.001
		Dry season soil moisture	5.9	8.48	<0.001
		Mean temperature	2.7	3.87	<0.001
		Total precipitation	2.6	3.79	<0.001
	Late	CO_2	30.3	40.99	<0.001
		Total precipitation	9.4	12.74	<0.001
		Mean VPD	9.0	12.23	<0.001
		ET/Precip ratio	8.5	11.45	<0.001
		Dry season soil moisture	6.5	8.83	<0.001
		Mean soil moisture	4.3	5.85	<0.001
		Wet season soil moisture	2.8	3.74	<0.001
		Mean temperature	2.5	3.41	<0.001
Total NEP	Early	Mean temperature	40.9	51.00	<0.001
		ET/Precip ratio	16.6	20.67	<0.001
		Total precipitation	12.5	15.64	<0.001

		Dry season soil moisture	8.1	10.12	<0.001
		CO_2	6.7	8.34	<0.001
	Mid	ET/Precip ratio	30.2	15.38	<0.001
		CO_2	19.8	10.09	<0.001
		Total precipitation	12.1	6.16	<0.001
		Mean VPD	5.4	2.75	<0.001
		Dry season soil moisture	3.6	1.85	<0.001
		Mean soil moisture	2.6	1.32	0.016
	Late	ET/Precip ratio	10.4	12.39	<0.001
		Mean soil moisture	8.2	9.78	<0.001
		Mean temperature	8.0	9.53	<0.001
		Dry season soil moisture	5.4	6.47	<0.001
		Total precipitation	5.2	6.18	<0.001
		Mean VPD	1.5	1.84	0.002
		Heat stress months	0.8	0.99	0.012
WUE	Early	Total precipitation	37.4	36.22	<0.001
		Mean temperature	14.7	14.23	<0.001
		CO_2	14.5	13.99	<0.001
		Mean VPD	3.9	3.78	<0.001
		Dry season soil moisture	1.3	1.27	0.004
	Mid	Total precipitation	53.3	69.70	<0.001
		CO_2	12.8	16.70	<0.001
		ET/Precip ratio	9.1	11.83	<0.001
		Dry season soil moisture	5.1	6.64	<0.001
		Heat stress months	3.5	4.56	<0.001
		Mean VPD	2.2	2.86	<0.001
	Late	Total precipitation	27.4	51.77	<0.001
		Dry season soil moisture	2.6	4.84	<0.001
		Wet season soil moisture	2.4	4.49	<0.001
		Mean temperature	1.3	2.55	0.003
		Heat stress months	0.3	0.59	0.041

Table S4. Driver interaction importance (GAM tensor product interactions, AR1-corrected). Variance explained by interaction terms (tensor product smooths) for each response variable across three time periods. Only significant interactions ($p < 0.05$) shown, sorted by variance explained. Models include first-order autoregressive (AR1) residual correlation structure grouped by simulation run.

Response	*Period*	*Interaction*	*Var. Expl. (%)*	*F*	*p-value*
Mean DBH	Early	CO_2 × Dry season SM	3.0	8.41	<0.001
		CO_2 × VPD	2.2	6.18	<0.001
		Heat stress × Dry season SM	0.9	2.44	<0.001
		CO_2 × ET/Precip	0.9	2.41	<0.001
	Mid	CO_2 × VPD	3.0	8.26	<0.001
		Temperature × Precipitation	0.6	1.76	<0.001
		Heat stress × Dry season SM	0.6	1.75	<0.001
		CO_2 × ET/Precip	0.2	0.76	0.006
		CO_2 × Mean SM	0.1	0.26	0.043
	Late	Heat stress × Dry season SM	21.0	19.35	<0.001
		Temperature × Precipitation	14.8	13.67	<0.001
		CO_2 × Mean SM	7.3	6.75	<0.001
		CO_2 × VPD	4.1	3.73	<0.001
		CO_2 × Dry season SM	2.1	1.91	<0.001
		CO_2 × ET/Precip	0.9	0.85	0.006
		Precipitation × ET/Precip	0.5	0.46	0.022
Mean AGB	Early	CO_2 × VPD	8.2	10.53	<0.001
		Heat stress × Dry season SM	3.3	4.21	<0.001
		CO_2 × Dry season SM	2.6	3.37	<0.001
		CO_2 × ET/Precip	0.9	1.18	0.001
		CO_2 × Mean SM	0.3	0.38	0.025
	Mid	Heat stress × Dry season SM	10.3	7.31	<0.001
		Temperature × Precipitation	8.6	6.14	<0.001
		CO_2 × Dry season SM	3.3	2.33	<0.001
		CO_2 × ET/Precip	2.8	2.03	<0.001
		Precipitation × ET/Precip	1.1	0.86	0.004
	Late	Heat stress × Dry season SM	25.0	13.48	<0.001
		Temperature × Precipitation	11.9	6.44	<0.001

		CO_2 × Mean SM	9.2	4.99	<0.001
		CO_2 × ET/Precip	4.3	2.29	<0.001
		CO_2 × VPD	2.6	1.43	<0.001
		CO_2 × Dry season SM	1.4	0.78	<0.001
		Precipitation × ET/Precip	0.9	0.46	0.011
AGB Growth	Early	CO_2 × Mean SM	5.1	1.78	<0.001
		CO_2 × VPD	2.9	1.04	0.002
		CO_2 × ET/Precip	2.9	1.01	0.001
		Temperature × Precipitation	2.9	1.01	0.004
	Mid	CO_2 × ET/Precip	6.9	2.30	<0.001
		CO_2 × Dry season SM	1.4	0.47	0.008
		Precipitation × ET/Precip	1.1	0.35	0.049
	Late	CO_2 × ET/Precip	10.7	4.45	<0.001
		Heat stress × Dry season SM	9.6	4.00	<0.001
		CO_2 × Mean SM	9.6	3.98	<0.001
		Temperature × Precipitation	4.6	1.90	<0.001
		CO_2 × VPD	4.2	1.76	<0.001
Mean LAI	Early	CO_2 × VPD	7.0	6.48	<0.001
		Precipitation × ET/Precip	1.4	1.33	<0.001
		Heat stress × Dry season SM	0.4	0.37	0.025
	Mid	CO_2 × VPD	13.2	8.46	<0.001
		Heat stress × Dry season SM	8.1	5.17	<0.001
		Temperature × Precipitation	5.6	3.59	<0.001
		CO_2 × Dry season SM	3.4	2.20	<0.001
		CO_2 × ET/Precip	2.4	1.57	<0.001
		Precipitation × ET/Precip	0.9	0.61	0.011
	Late	Heat stress × Dry season SM	11.4	6.86	<0.001
		Temperature × Precipitation	8.2	4.94	<0.001
		CO_2 × VPD	2.5	1.47	<0.001
		CO_2 × Mean SM	2.4	1.42	<0.001
		CO_2 × ET/Precip	1.3	1.03	0.007
		Precipitation × ET/Precip	0.4	0.26	0.049
Total NEP	Early	CO_2 × VPD	5.8	3.24	<0.001

		CO_2 × Dry season SM	4.8	2.67	<0.001
		Temperature × Precipitation	3.3	1.83	<0.001
		Heat stress × Dry season SM	0.6	0.35	0.031
	Mid	Temperature × Precipitation	10.2	2.30	<0.001
		Precipitation × ET/Precip	7.5	1.71	<0.001
		CO_2 × VPD	3.2	0.73	0.017
		CO_2 × Dry season SM	1.8	0.41	0.030
		Heat stress × Dry season SM	1.6	0.36	0.031
	Late	CO_2 × Dry season SM	20.4	10.79	<0.001
		Heat stress × Dry season SM	15.7	8.34	<0.001
		Temperature × Precipitation	15.3	8.10	<0.001
		CO_2 × VPD	4.7	2.50	<0.001
		CO_2 × Mean SM	4.2	2.24	<0.001
WUE	Early	Precipitation × ET/Precip	10.1	4.35	<0.001
		Temperature × Precipitation	8.1	3.47	<0.001
		CO_2 × VPD	4.8	2.07	<0.001
		CO_2 × Dry season SM	3.3	1.43	<0.001
		Heat stress × Dry season SM	0.9	0.39	0.040
	Mid	Temperature × Precipitation	7.5	4.38	<0.001
		CO_2 × Dry season SM	2.3	1.32	<0.001
		Heat stress × Dry season SM	2.0	1.16	<0.001
		CO_2 × VPD	1.7	1.01	0.003
	Late	Temperature × Precipitation	21.3	17.90	<0.001
		Heat stress × Dry season SM	18.6	15.59	<0.001
		CO_2 × Mean SM	16.1	13.48	<0.001
		Precipitation × ET/Precip	6.7	5.61	<0.001
		CO_2 × Dry season SM	1.4	1.14	<0.001
		CO_2 × VPD	1.3	1.12	0.007
		CO_2 × ET/Precip	0.4	0.30	0.046

B2. Drought Sensitivity

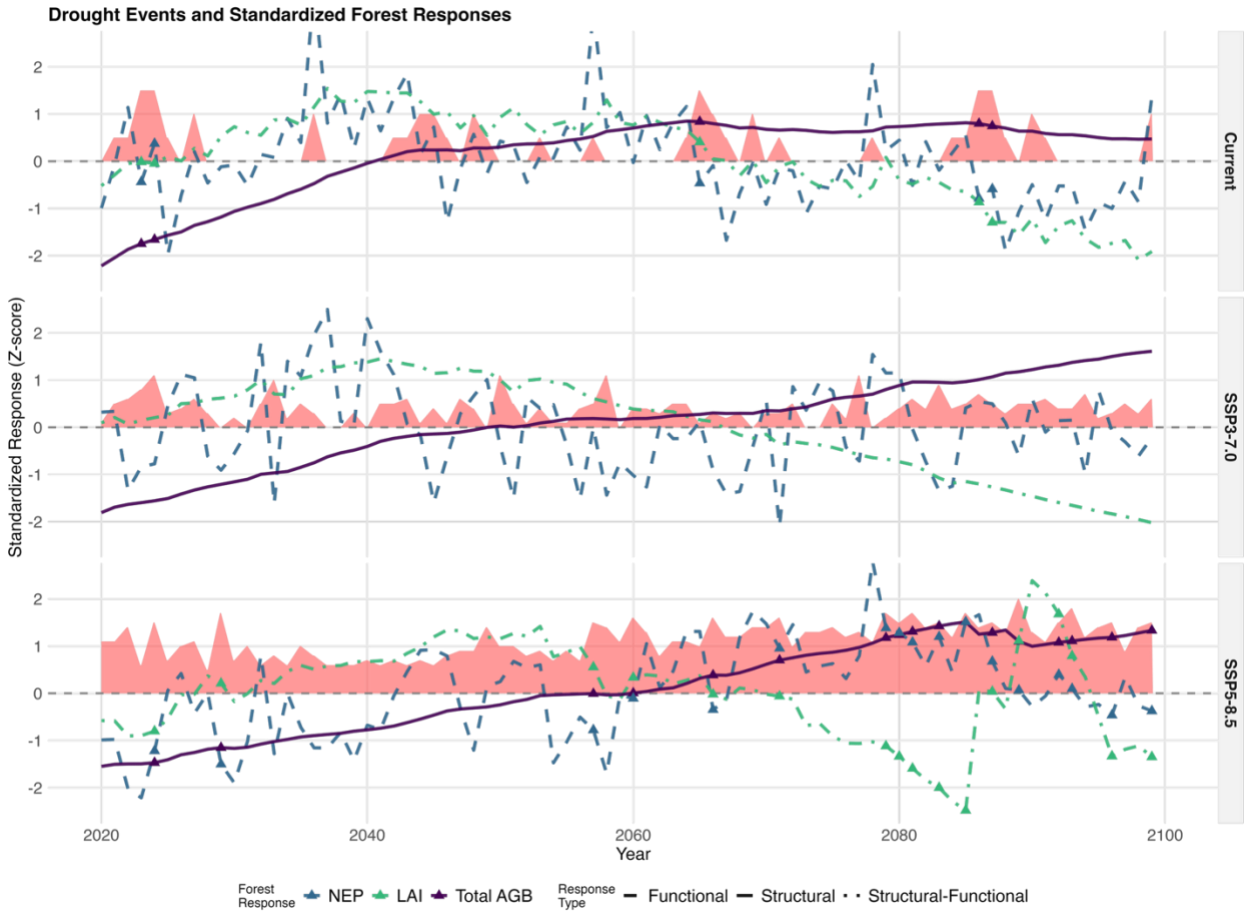

Figure S12. Drought events and standardized forest responses across climate scenarios (2020-2099). Red areas indicate drought severity (scaled 0-2.5), triangles mark severe drought events (≥3 severity), and colored lines show standardized responses of forest responses. NEP (functional, dashed blue) exhibits the highest drought sensitivity, followed by LAI (structural-functional, dot-dash green), while AGB (structural, solid purple) shows the lowest sensitivity with greater inertia. Forest responses are standardized within each scenario to enable comparison across variables with different units.

B3. CO_2 Fertilization Effects

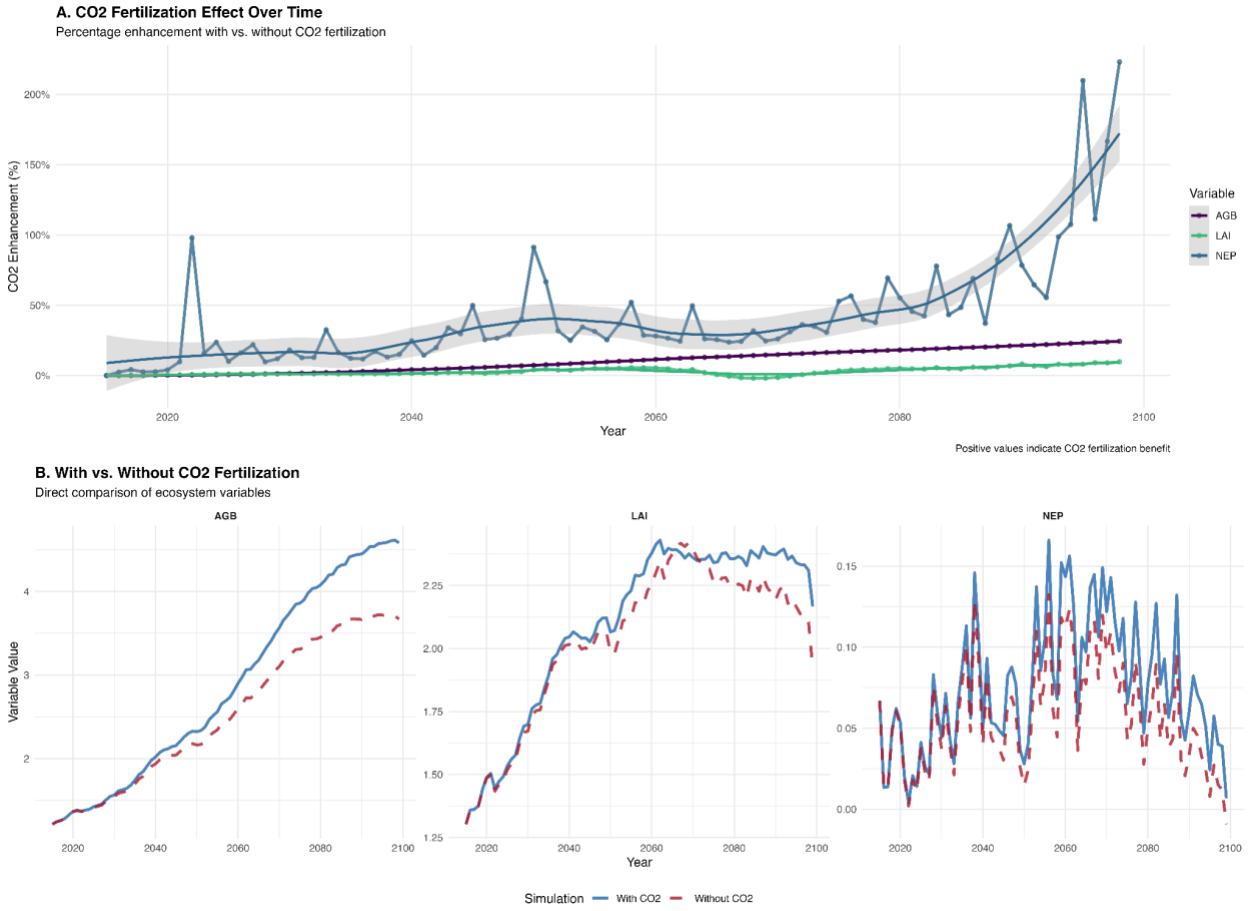

Figure S13. CO2 fertilization effects on forest ecosystem responses under SSP3-7.0, Model ipsl-cm6a-lr. (A) Percentage enhancement over time showing increasing CO2 fertilization benefits, with NEP exhibiting the strongest response (up to 200% enhancement), followed by moderate AGB enhancement (~20%) and minimal LAI response (~5%). (B) Direct comparison of absolute values demonstrates diverging trajectories between simulations with (solid blue) and without (dashed red) CO2 fertilization.

Table S5. Percentage enhancement from CO2 fertilization by time period, showing escalating benefits particularly for ecosystem productivity (NEP: 16% → 67%) versus structure (AGB: 1% → 20%).

Period	AGB Enhancement	LAI Enhancement	NEP Enhancement
Early Century	1.4%	0.9%	16.2%
Mid Century	9.6%	2.6%	33.5%
Late Century	19.9%	5.7%	66.9%

B4.CO_2 Fertilization Constraint for Mediterranean Drylands

To represent realistic CO_2 responses in water-limited systems, we implemented a saturating fertilization constraint based on empirical observations from Free-Air CO_2 Enrichment (FACE) experiments in Mediterranean and dryland ecosystems. The constraint reflects the finding that CO_2 enhancement of photosynthesis and growth is substantially smaller in water-limited systems compared to mesic environments, and that benefits saturate at moderate CO_2 levels due to nutrient, hydraulic, and acclimation constraints (Leuzinger & Körner, 2007; De Kauwe et al., 2013; Terrer et al., 2019).

Implementation

We applied a maximum 15% enhancement of photosynthetic capacity and stomatal efficiency under elevated CO_2. This value is intermediate between extreme desert systems (0% response) and mesic forests/woodlands (23% response; Norby et al., 2010), reflecting the moderate water limitation at Yatir. The constraint follows a Michaelis-Menten saturation function with half-saturation at 550 ppm:

$$CO_2\_effect = 1.0 + 0.15 \times (CO_2\_ratio - 1.0) / ((CO_2\_ratio - 1.0) + 0.375)$$

where CO_2_ratio = atmospheric CO_2 / 400 ppm (current climate baseline).

The half-saturation point of 550 ppm was chosen to match typical FACE experimental CO_2 enrichment levels (e.g., +200 ppm above ambient), representing the transition from linear CO_2 response to saturation. At 550 ppm (CO_2_ratio = 1.375), the function yields ~56% of maximum enhancement (8.4% total increase); at 800 ppm, the enhancement reaches ~88% of maximum (13.2% total increase), approaching the 15% ceiling.

This scaling factor is applied to all photosynthetic parameters:
- Maximum carboxylation rate: $V_{cmax} = V_{cmax,base} \times CO_2\_effect$
- Maximum electron transport rate: $J_{max} = J_{max,base} \times CO_2\_effect$
- Maximum triose phosphate utilization rate: $TPm = TPm_{,base} \times CO_2\_effect$
- Stomatal optimization parameter: $\lambda = \lambda_{base} \times CO_2\_effect$

Interaction with Hydraulic Constraints

The CO_2 constraint operates in sequence with water stress effects via the hydraulic module (h2o_plant_lim = 4). After CO_2 enhancement is applied, additional hydraulic limitations reduce photosynthetic capacity and stomatal conductance based on leaf water potential (ψleaf) relative to the turgor loss point (ψTLP):

$$\text{Water stress factor} = \max(10^{-6}, \min(1.0, 1 / (1 + 0.1 \times (\psi leaf / \psi TLP)^{6})))$$

This factor is applied to electron transport rate (J_{max}) and quantum efficiency (α), representing reduced ATP synthase activity under water stress (Tezara et al., 2001). Stomatal sensitivity to vapor pressure deficit also increases with water stress through an exponential scaling of λ (Manzoni et al., 2011):

$$\lambda_{drought} = \lambda \times \exp(\beta \times \max(\psi leaf - \psi leaf,min))$$

where β is a species-specific stomatal sensitivity parameter and ψleaf,min is the minimum sustainable leaf water potential.

This two-stage approach ensures that:
1. CO_2 benefits saturate at moderate atmospheric CO_2 levels (~550-700 ppm)
2. Remaining benefits are further suppressed under drought stress
3. Stomatal responses to CO_2 and water stress interact realistically

Justification

This parameterization is consistent with:
- FACE experiments showing 0-23% growth enhancement across aridity gradients, with water-limited sites at the lower end (Norby et al., 2010; De Kauwe et al., 2013)
- Meta-analyses demonstrating nutrient and water co-limitation of CO_2 fertilization (Terrer et al., 2019; Walker et al., 2021)
- Mediterranean field observations showing minimal long-term CO_2 effects under persistent drought (Ogaya & Peñuelas, 2021)
- Physiological evidence for photosynthetic downregulation and acclimation under prolonged CO_2 enrichment in water-limited systems (Leuzinger & Körner, 2007)

Without this constraint, simulated productivity under elevated CO_2 would be unrealistically high and linearly increasing, contrary to empirical evidence from Mediterranean drylands. The constraint allows early-century CO_2 benefits (when atmospheric CO_2 is 400-500 ppm and water stress is moderate) while preventing overestimation of long-term carbon sequestration as CO_2 rises further and climate stress intensifies.

C1. Climate Data and Processing

This appendix describes the climate input data, including bias correction procedures for precipitation, temporal downscaling methods, and statistical analyses of drought severity across climate scenarios.

C1.1. Climate Projections

Projected climate trajectories across all five models consistently indicate a shift towards more frequent and severe droughts throughout the 21st century, particularly under SSP5-8.5. While mean annual precipitation (MAP) declines steadily in most models, the largest reductions occur under SSP3-7.0 (Tables S6,7; Fig. 1a). In SSP5-8.5, however, MAP declines are less consistent across models, which instead show an increasing occurrence of both extreme dry and extreme wet years, reflecting growing hydroclimatic variability.

Precipitation drought frequency increases sharply across all future scenarios. Whereas drought years (total precipitation <200 mm) occurred in ~7% of years under current climate conditions, their frequency rises to 20% under SSP3-7.0 and up to 34% under SSP5-8.5 (Table S6, S7). Severe precipitation droughts (<150 mm) become even more frequent, tripling in occurrence under SSP5-8.5 relative to the current scenario.

In addition to higher precipitation drought frequency, models project longer dry spells, characterised by a drastic reduction of the length of the rainy season and greater clustering of consecutive drought years (Table S4).

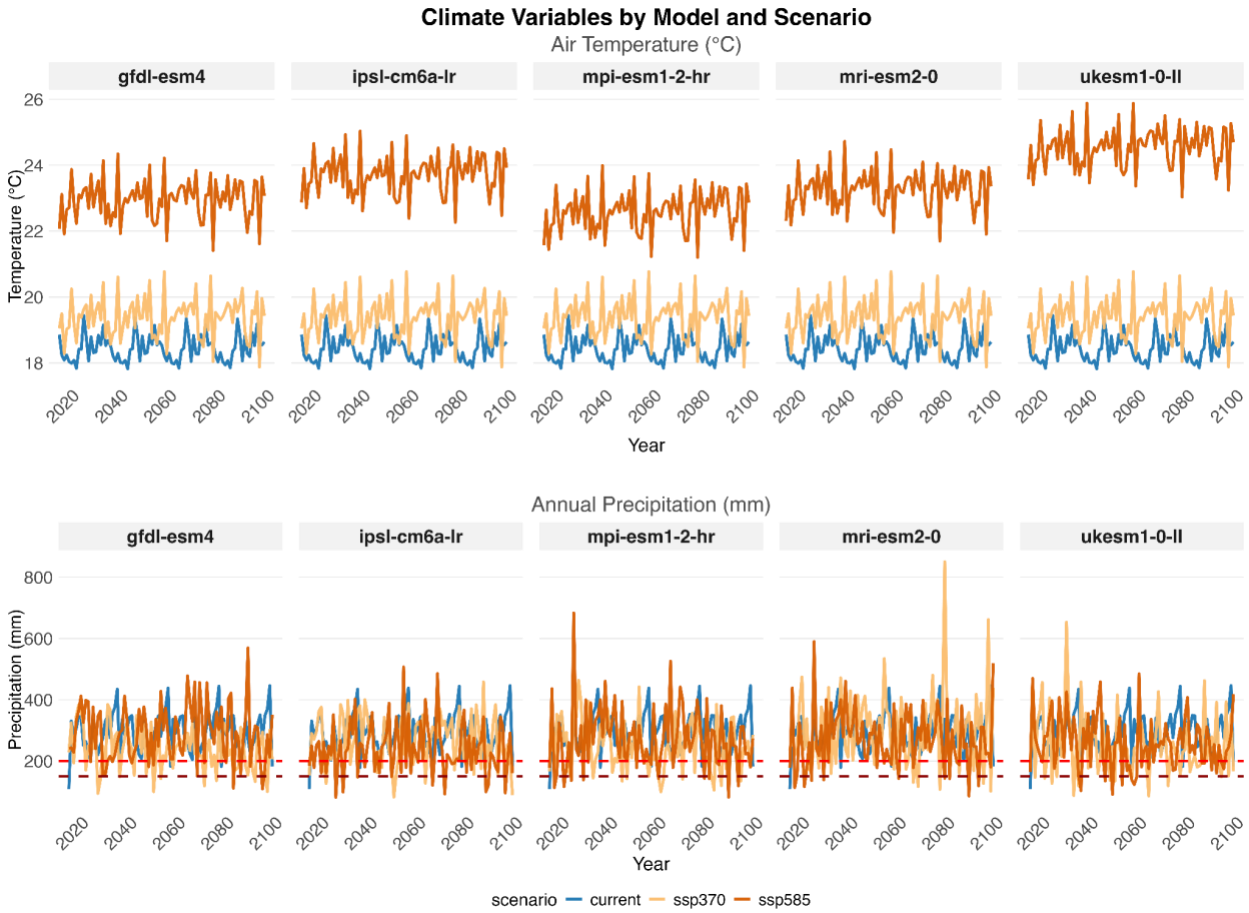

Figure S14. Projected temperature (top row, °C) and precipitation (bottom row, mm yr^{-1}) across global climate models (current: blue; SSP3-7.0: orange; SSP5-8.5: red) from 2015–2100. Warming intensifies across both SSP trajectories, while precipitation declines are most consistent under SSP3-7.0 but exhibit greater interannual variability under SSP5-8.5. In the precipitation subfigure, the red dashed line represents the moderate drought threshold (mean annual precipitation <200 mm) and the dark red dashed line represents the severe drought threshold (<150 mm).

C1.2. Temporal Evolution of Drought Severity Within Climate Scenarios

Statistical analysis of drought severity distributions across time periods (2015-2040, 2041-2070, 2071-2099) revealed distinct temporal evolution patterns for each climate scenario. Under current climate conditions, drought severity showed no significant temporal trend (Kruskal-Wallis $\chi^2 = 2.74$, $p = 0.25$), with severe drought frequency remaining stable at 3.8-6.9% across all periods, indicating natural climate variability without systematic intensification (Fig. 2).

In contrast, both future warming scenarios exhibited significant temporal changes in drought patterns. The SSP3-7.0 scenario showed significant drought intensification over time (Fig. 2, $\chi^2 = 11.0$, $p = 0.004$), with mean drought severity increasing by 62% from early (0.60) to late century (0.97). Post-hoc analysis revealed that this intensification was primarily driven by late-century acceleration, with significant differences between early and late periods ($p = 0.0035$) and between

mid and late periods ($p = 0.012$). Correspondingly, the frequency of severe drought events more than doubled from 6.9% in early century to 16.6% in late century.

The SSP5-8.5 scenario demonstrated the most dramatic temporal changes ($\chi^2 = 76.6$, $p < 0.001$), with all time periods differing significantly from each other (all pairwise comparisons $p \leq 0.005$). Mean drought severity increased by 59% from early (1.76) to late century (2.80), while severe drought frequency more than doubled from 20% to 45.5%. Unlike SSP3-7.0, this high-warming scenario showed continuous intensification throughout the century rather than late-period acceleration, indicating sustained and accelerating drought stress under extreme climate change conditions.

These results demonstrate that climate change fundamentally alters drought temporal dynamics, transitioning from stable patterns under current conditions to gradual intensification under moderate warming and continuous escalation under high warming scenarios.

C1.3. Between-Scenario Differences in Drought Severity and Composition

Statistical comparison of drought severity distributions revealed highly significant differences between climate scenarios across all time periods (Fig. 1, Kruskal-Wallis $\chi^2 = 346.13$, $p < 0.001$). Post-hoc pairwise comparisons using Dunn's test with Bonferroni correction showed that while current climate and SSP3-7.0 scenarios did not differ significantly ($p = 0.39$), both differed dramatically from SSP5-8.5 (both $p < 0.001$). The SSP5-8.5 scenario exhibited a 277% increase in mean drought severity (2.22) compared to current conditions (0.59) and a 196% increase relative to SSP3-7.0 (0.75).

The probability of severe to extreme drought events (severity ≥ 3) increased substantially across scenarios, rising from 4.7% under current climate to 10.4% under SSP3-7.0 (2.2-fold increase) and 31.5% under SSP5-8.5 (6.7-fold increase). This represents a fundamental shift in drought risk, with SSP5-8.5 exhibiting severe drought probabilities nearly an order of magnitude higher than current climate conditions.

Drought composition patterns also differed significantly between scenarios ($\chi^2 = 842.98$, $p < 0.001$). Under current climate, VPD-dominated drought events comprised only 4.7% of all years, with the modal drought severity being zero (no drought). SSP3-7.0 showed minimal change in VPD dominance (4.5%), maintaining similar compositional patterns to the current climate. In stark contrast, SSP5-8.5 exhibited a complete compositional shift, with VPD-dominated drought events occurring in 99.8% of years and the modal drought severity shifting to level 2 (moderate drought), indicating that atmospheric drought becomes the predominant stress factor under high warming conditions.

Period-specific analyses confirmed that scenario differences were consistent across all time periods, with significant differences in both drought severity distributions and component dominance patterns for early century (severity: $\chi^2 = 102$, $p < 0.001$; composition: $\chi^2 = 263$, $p < 0.001$), mid century ($\chi^2 = 122$ and 303, both $p < 0.001$), and late century ($\chi^2 = 140$ and 278, both $p < 0.001$). These findings

demonstrate that climate scenario differences in drought characteristics are robust across temporal scales and represent fundamental shifts in drought regimes rather than transient variations.

Table S6: Climate characteristics and drought frequencies across models and scenarios. The values represent the ensemble means (bold) followed by individual models ordered by severe precipitation drought frequency. Drought years were defined by annual precipitation: ≤200 mm for drought and <150 mm for severe drought. Climate variables are calculated via hydrological years (October--September) for 2080--2099. The current observed data represent 2000--2020. The arrows indicate the direction and magnitude of change from the current observed values: ↑↑ = >+50%, ↑ = +10--50%, → = ±10%, ↓ = -10--50%, ↓↓ = <-50%.

Scenario	Model	Number of Drought Years	Number of Severe Drought Years	MAT [°C]	Rainy Season Length [days]	MAP [mm]
Current	**Observed**	**6**	**2**	**18.5**	**166**	**282.8**
SSP3-7.0	**Ensemble Mean**	**23 ↑↑**	**9 ↑↑**	**19.4 ↑**	**144 ↓**	**251 ↓**
	ipsl-cm6a-lr	19 ↑	5 ↑	19.4 ↑	140 ↓	265 →
	mri-esm2-0	17 ↑	6 ↑	19.4 ↑	155 →	300 ↑
	gfdl-esm4	25 ↑↑	10 ↑↑	19.4 ↑	140 ↓	216 ↓
	mpi-esm1-2-hr	26 ↑↑	13 ↑↑	19.4 ↑	143 ↓	226 ↓

	ukes1-0-ll	28 ↑↑	13 ↑↑	19.4 ↑	143 ↓	248 ↓
SSP5-8.5	**Ensemble Mean**	**23 ↑↑**	**8 ↑↑**	**23.5 ↑↑**	**144 ↓**	**244 ↓**
	gfdl-esm4	19 ↑	3 →	23.0 ↑↑	145 ↓	264 →
	ukes1-0-ll	26 ↑↑	8 ↑↑	24.6 ↑↑	148 ↓	239 ↓
	ipsl-cm6a-lr	29 ↑↑	10 ↑↑	23.8 ↑↑	136 ↓	220 ↓
	mpi-esm1-2-hr	21 ↑	10 ↑↑	22.8 ↑↑	145 ↓	243 ↓
	mri-esm2-0	21 ↑	10 ↑↑	23.3 ↑↑	147 ↓	254 →

Table S7. Summary statistics of drought severity distributions across climate scenarios and temporal periods. Values represent percentages of years in each drought category and mean drought severity on a 0-5 scale.

Climate Scenario	Time Period	Mean Severity	No Drought (%)	Mild (%)	Moderate (%)	Severe (%)	Extreme (%)	VPD-Dominated (%)
Current	Early Century	0.42	73.1	15.4	7.7	3.8	0.0	3.8

Current	Mid Century	0.73	50.0	30.0	16.7	3.3	0.0	6.7
Current	Late Century	0.59	65.5	17.2	10.3	6.9	0.0	3.4
SSP3-7.0	Early Century	0.60	63.8	19.2	10.0	6.9	0.0	3.1
SSP3-7.0	Mid Century	0.66	61.3	21.3	10.0	7.3	0.0	3.3
SSP3-7.0	Late Century	0.97	46.2	27.6	9.7	15.9	0.7	6.9
SSP5-8.5	Early Century	1.76	21.5	31.5	40.0	6.9	0.0	99.2
SSP5-8.5	Mid Century	2.05	14.0	25.3	41.3	19.3	0.0	100.0
SSP5-8.5	Late Century	2.80	8.3	20.7	46.2	24.1	0.7	100.0

C2. Climate input data: sources, bias correction, and temporal downscaling.

C2.1. Bias Correction of Precipitation Data

Given the critical importance of accurate precipitation representation for dryland forest modeling, we applied bias correction to the daily precipitation data from the CMIP6 reanalysis by (Gebrechorkos et al. (2023). While this dataset provides improved spatial resolution (0.25°) and regional representation compared to standard GCM outputs, systematic biases can still significantly affect simulated ecosystem responses, particularly for water-limited systems where small changes in rainfall patterns can have disproportionate impacts on forest productivity and survival.

We employed robust quantile mapping (RQM) to correct precipitation data from the five CMIP6 models under two emission scenarios, using observed hourly precipitation from the Israeli Meteorological Service (IMS) for 1998–2014 as the reference dataset. RQM adjusts the entire cumulative distribution function (CDF) of simulated precipitation to match that of observations, ensuring that both central tendencies and extreme values are appropriately corrected.

The bias correction procedure was implemented using the qmap R package following a two-step process: (i) the fitQmapQUANT function estimated quantile mapping parameters based on the historical overlap period (1998–2014), establishing transfer functions between the Gebrechorkos et al. (2023) reanalysis and observed precipitation distributions; and (ii) the doQmapQUANT function applied these corrections to both historical and future simulated data, preserving relative changes in precipitation patterns while removing systematic biases.

This approach maintains the statistical properties of precipitation extremes, including drought frequency, intensity, and duration, which are particularly important for assessing forest resilience under climate change.

C2.2. Temporal downscaling of climate forcings

To capture sub-daily variations in physiological processes and preserve realistic diurnal cycles of carbon and water fluxes (Shuai et al., 2022), we downscaled daily GCM outputs to hourly resolution using variable-specific statistical methods. Temporal downscaling requires both high-resolution control data and the coarser-resolution target dataset to be downscaled.

We used 15–25 years of hourly observational data as control datasets, combining records from the Israeli Meteorological Service (IMS) with on-site measurements from an eddy covariance flux tower at Yatir Forest. This duration provides sufficient temporal coverage to capture interannual climate variability and long-term trends while maintaining statistical robustness (Michel et al., 2021).

Different meteorological variables required tailored downscaling approaches based on their statistical properties and physical characteristics. For air temperature, we applied the additive delta method with Fourier series smoothing to preserve realistic diurnal temperature cycles. Specific humidity, air pressure, wind speed, and radiation components (shortwave and longwave) were downscaled using the multiplicative delta method to maintain proportional relationships and prevent unrealistic negative values.

Precipitation temporal downscaling presented unique challenges due to its intermittent, highly variable nature and the critical importance of extreme events for dryland ecosystem dynamics. We employed a Weather Generator approach that stochastically simulates hourly precipitation sequences based on statistical relationships derived from observed data and large-scale climate patterns (Michel et al., 2021). This method preserves key precipitation characteristics including seasonality, dry spell duration, and the occurrence of extreme events, all critical factors for simulating dryland forest water stress and recovery dynamics.

References

Antonarakis, A. S., Bogan, S. A., Goulden, M. L., & Moorcroft, P. R. (2022). Impacts of the 2012–2015 Californian drought on carbon, water and energy fluxes in the Californian Sierras: Results from an imaging spectrometry-constrained terrestrial biosphere model. *Global Change Biology*, *28*(5), 1823–1852. https://doi.org/10.1111/gcb.15995

Choat, B., Brodribb, T. J., Brodersen, C. R., Duursma, R. A., López, R., & Medlyn, B. E. (2018). Triggers of tree mortality under drought. *Nature*, *558*(7711), 531–539. https://doi.org/10.1038/s41586-018-0240-x

Gebrechorkos, S., Leyland, J., Slater, L., Wortmann, M., Ashworth, P. J., Bennett, G. L., Boothroyd, R., Cloke, H., Delorme, P., Griffith, H., Hardy, R., Hawker, L., McLelland, S., Neal, J., Nicholas, A., Tatem, A. J., Vahidi, E., Parsons, D. R., & Darby, S. E. (2023). A high-resolution daily global dataset of statistically downscaled CMIP6 models for climate impact analyses. *Scientific Data*, *10*(1), 611. https://doi.org/10.1038/s41597-023-02528-x

Grünzweig, J. M., Lin, T., Rotenberg, E., Schwartz, A., & Yakir, D. (2003). Carbon sequestration in arid-land forest. *Global Change Biology*, *9*(5), 791–799. https://doi.org/10.1046/j.1365-2486.2003.00612.x

Johnston, M. (2021). *Plant temperature in a Mediterranean woodland savanna: Measurements and models*. Thesis, Harvard University. https://dash.harvard.edu/handle/1/37368432

Klein, T. (2021). Carbon Allocation Dynamics in Mediterranean Pines Under Stress. In G. Ne'eman & Y. Osem (Eds), *Pines and Their Mixed Forest Ecosystems in the Mediterranean Basin* (pp. 117–128). Springer International Publishing. https://doi.org/10.1007/978-3-030-63625-8_7

Klein, T., Cohen, S., & Yakir, D. (2011). Hydraulic adjustments underlying drought resistance of Pinus halepensis. *Tree Physiology*, *31*(6), 637–648. https://doi.org/10.1093/treephys/tpr047

Klein, T., Rotenberg, E., Cohen-Hilaleh, E., Raz-Yaseef, N., Tatarinov, F., Preisler, Y., Ogée, J., Cohen, S., & Yakir, D. (2014). Quantifying transpirable soil water and its relations to tree water use dynamics in a water-limited pine forest. *Ecohydrology*, *7*(2), 409–419. https://doi.org/10.1002/eco.1360

Lapidot, O., Ignat, T., Rud, R., Rog, I., Alchanatis, V., & Klein, T. (2019). Use of thermal imaging to detect evaporative cooling in coniferous and broadleaved tree species of the

Mediterranean maquis. *Agricultural and Forest Meteorology*, *271*, 285–294. https://doi.org/10.1016/j.agrformet.2019.02.014

Llusia, J., Roahtyn, S., Yakir, D., Rotenberg, E., Seco, R., Guenther, A., & Peñuelas, J. (2016). Photosynthesis, stomatal conductance and terpene emission response to water availability in dry and mesic Mediterranean forests. *Trees*, *30*(3), 749–759. https://doi.org/10.1007/s00468-015-1317-x

Maseyk, K., Grünzweig, J. M., Rotenberg, E., & Yakir, D. (2008). Respiration acclimation contributes to high carbon-use efficiency in a seasonally dry pine forest. *Global Change Biology*, *14*(7), 1553–1567. https://doi.org/10.1111/j.1365-2486.2008.01604.x

Michel, A., Sharma, V., Lehning, M., & Huwald, H. (Eds). (2021). Climate change scenarios at hourly time-step over Switzerland from an enhanced temporal downscaling approach. *International Journal of Climatology*. https://doi.org/10.1002/joc.7032

Norby, R. J., Warren, J. M., Iversen, C. M., Medlyn, B. E., & McMurtrie, R. E. (2010). CO2 enhancement of forest productivity constrained by limited nitrogen availability. *Proceedings of the National Academy of Sciences*, *107*(45), 19368–19373. https://doi.org/10.1073/pnas.1006463107

Osem, Y., & O'Hara, K. (2016). An ecohydrological approach to managing dryland forests: Integration of leaf area metrics into assessment and management. *Forestry: An International Journal of Forest Research*, *89*(4), 338–349. https://doi.org/10.1093/forestry/cpw021

Pandit, K., Dashti, H., Glenn, N. F., Flores, A. N., Maguire, K. C., Shinneman, D. J., Flerchinger, G. N., & Fellows, A. W. (2019). Developing and optimizing shrub parameters representing sagebrush (*Artemisia* spp.) ecosystems in the northern Great Basin using the Ecosystem Demography (EDv2.2) model. *Geoscientific Model Development*, *12*(11), 4585–4601. https://doi.org/10.5194/gmd-12-4585-2019

Pastorello, G., Trotta, C., Canfora, E., Chu, H., Christianson, D., Cheah, Y.-W., Poindexter, C., Chen, J., Elbashandy, A., Humphrey, M., Isaac, P., Polidori, D., Reichstein, M., Ribeca, A., van Ingen, C., Vuichard, N., Zhang, L., Amiro, B., Ammann, C., … Papale, D. (2020). The FLUXNET2015 dataset and the ONEFlux processing pipeline for eddy covariance data. *Scientific Data*, *7*(1), 225. https://doi.org/10.1038/s41597-020-0534-3

Piper, F. I., & Fajardo, A. (2016). Carbon dynamics of Acer pseudoplatanus seedlings under drought and complete darkness. *Tree Physiology*, *36*(11), 1400–1408. https://doi.org/10.1093/treephys/tpw063

Preisler, Y., Tatarinov, F., Grünzweig, J. M., Bert, D., Ogée, J., Wingate, L., Rotenberg, E., Rohatyn, S., Her, N., Moshe, I., Klein, T., & Yakir, D. (2019). Mortality versus survival in drought-affected Aleppo pine forest depends on the extent of rock cover and soil stoniness. *Functional Ecology*, *33*(5), 901–912. https://doi.org/10.1111/1365-2435.13302

Qubaja, R., Grünzweig, J. M., Rotenberg, E., & Yakir, D. (2020). Evidence for large carbon sink and long residence time in semiarid forests based on 15 year flux and inventory records. *Global Change Biology*, *26*(3), 1626–1637. https://doi.org/10.1111/gcb.14927

Raz-Yaseef, N., Yakir, D., Schiller, G., & Cohen, S. (2012). Dynamics of evapotranspiration partitioning in a semi-arid forest as affected by temporal rainfall patterns. *Agricultural and Forest Meteorology*, *157*, 77–85. https://doi.org/10.1016/j.agrformet.2012.01.015

Rog, I., Tague, C., Jakoby, G., Megidish, S., Yaakobi, A., Wagner, Y., & Klein, T. (2021). Interspecific Soil Water Partitioning as a Driver of Increased Productivity in a Diverse Mixed Mediterranean Forest. *Journal of Geophysical Research: Biogeosciences*, *126*(9), e2021JG006382. https://doi.org/10.1029/2021JG006382

Rotenberg, E., & Yakir, D. (2010). Contribution of Semi-Arid Forests to the Climate System. *Science*, *327*(5964), 451–454. https://doi.org/10.1126/science.1179998

Sprintsin, M., Cohen, S., Maseyk, K., Rotenberg, E., Grünzweig, J., Karnieli, A., Berliner, P., & Yakir, D. (2011). Long term and seasonal courses of leaf area index in a semi-arid forest plantation. *Agricultural and Forest Meteorology*, *151*(5), 565–574. https://doi.org/10.1016/j.agrformet.2011.01.001

Sprintsin, M., Karnieli, A., Berliner, P., Rotenberg, E., Yakir, D., & Cohen, S. (2007). The effect of spatial resolution on the accuracy of leaf area index estimation for a forest planted in the desert transition zone. *Remote Sensing of Environment*, *109*(4), 416–428. https://doi.org/10.1016/j.rse.2007.01.020

Terrer, C., Jackson, R. B., Prentice, I. C., Keenan, T. F., Kaiser, C., Vicca, S., Fisher, J. B., Reich, P. B., Stocker, B. D., Hungate, B. A., Peñuelas, J., McCallum, I., Soudzilovskaia, N. A., Cernusak, L. A., Talhelm, A. F., Van Sundert, K., Piao, S., Newton, P. C. D., Hovenden, M. J., … Franklin, O. (2019). Nitrogen and phosphorus constrain the CO2 fertilization of global plant biomass. *Nature Climate Change*, *9*(9), 684–689. https://doi.org/10.1038/s41558-019-0545-2

Zhang, J., Bras, R. L., Longo, M., & Heartsill Scalley, T. (2022). The impact of hurricane disturbances on a tropical forest: Implementing a palm plant functional type and hurricane disturbance module in ED2-HuDi V1.0. *Geoscientific Model Development*, *15*(13), 5107–5126. https://doi.org/10.5194/gmd-15-5107-2022

Zhu, Z., Zeng, H., Myneni, R. B., Chen, C., Zhao, Q., Zha, J., Zhan, S., & MacLachlan, I. (2021). Comment on “Recent global decline of CO2 fertilization effects on vegetation photosynthesis”. *Science*, *373*(6562), eabg5673. https://doi.org/10.1126/science.abg5673